EPFL

MASTER THESIS

Rapid Elastic Contact: Image Processing and the Virtual Frame Technique (VFT)

Author:
Siqi ZHENG

Supervisor:
Dr. John Martin KOLINSKI

*A thesis submitted in fulfillment of the requirements
for the degree of Master in Mechanical Engineering*

in the

School of Engineering

January 17, 2020

Declaration of Authorship

I, Siqi ZHENG, declare that this thesis titled, "Rapid Elastic Contact: Image Processing and the Virtual Frame Technique (VFT)" and the work presented in it are my own. I confirm that:

- This work was done wholly or mainly while in candidature for a research degree at this University.

- Where any part of this thesis has previously been submitted for a degree or any other qualification at this University or any other institution, this has been clearly stated.

- Where I have consulted the published work of others, this is always clearly attributed.

- Where I have quoted from the work of others, the source is always given. With the exception of such quotations, this thesis is entirely my own work.

- I have acknowledged all main sources of help.

- Where the thesis is based on work done by myself jointly with others, I have made clear exactly what was done by others and what I have contributed myself.

Signed: Siqi Zheng

Date: 17-01-2020

ÉCOLE POLYTECHNIQUE FÉDÉRALE DE LAUSANNE

Abstract

School of Engineering

Master in Mechanical Engineering

Rapid Elastic Contact: Image Processing and the Virtual Frame Technique (VFT)

by Siqi ZHENG

A central air bubble is observed to be maintained during the process of an elastic hemi-sphere impacting on a smooth rigid surface. The similar phenomenon has been found in droplet impact in other studies. The effect of air gap between the two solids has been always neglected in the previous studies of the impact problem. We find that the central air bubble has a big contribution to the energy loss in the second phase of impact process. Its negative pressure under the tensile force prevents the hemi-sphere impactor from rebounding from the surface. The impactor made of softer material or with a lower impact velocity often can lead to a larger initial size of central air bubble. But the high impact velocity can increase the negative pressure and the resistance brought by it. With high impact velocities and softer material, the propagation of outward contact can also become faster thanks to the decline of air defects and the disappearance of instability patterns. We guess that the air permeates into the tiny cracks on the impactor surface, which appear due to the high stress.

Acknowledgements

I would first like to thank my thesis supervisor Dr. John Martin KOLINSKI. He is very patient and knowledgeable, and always gives me good advice and guidance. I would also like to thank the lab members from Engineering Mechanics of Soft Interfaces (EMSI). Without their help and encouragement, this project would not have been completed successfully.

Contents

Chapter 1

Introduction

A ping-pong ball bouncing against the table, a marble toy hitting the ground and a particle striking the metal plate, all of these are contact problems of a sphere impacting on a flat surface. This impact event is a dynamic process, which can occur between the elastic solid and elastic solid, between rigid solid and rigid solid or between the elastic solid and rigid solid. The rate of loading, material properties and the curvature of sphere can affect the stress distribution and the deformation of solid (Johnson, 1985). Because of the stress singularity in contact problem between the rigid impactor and the rigid surface, nowadays the researches of impact dynamics discuss more about the elastic impactor or elastic surface. Contact mechanics is initially studied based on the assumption that the surface is smooth both on the microscopic scale and on the macroscopic scale. Later people found that surface roughness on the microscopic scale can lead to less actual contact area than the apparent contact area, and studied how decreased contact area change with the normal force (Bowden and Tabor, 1966; Persson, 2001). The transient stage from fully elastic contact to fully plastic contact aroused the attention, called elastic-plastic contact. Finite Element Method (FEM) is favored by people to model and analyze this transient stage in the contact problem either between the elastic half-space and rigid sphere or between the elastic sphere and rigid surface (Kral, Komvopoulos, and Bogy, 1993; Kogut and Etsion, 2002). Recently, the relevant researches have gone in depth based on the theories above and some entered more specific field. For instance, the behavior of RC (Reinforced Concrete) beam under impact(Cotsovos, Stathopoulos, and Zeris, 2008), the influence of layer number and air gap on the ballistic performance of the multi-layered substrate(Liu et al., 2018).

However, the effect of air gap between the sphere and substrate has been neglected in the previous studies, which in fact appears to be able to deform the elastic impactor (Dillavou, Rubinstein, and Kolinski, 2019). In the experiment of an impacting elastic hemi-sphere, a central air bubble is recorded by Virtual Frame Technique (VFT) to be maintained for the entire exposure (Dillavou, Rubinstein, and Kolinski, 2019). It is very similar to what happens in the experiment of the impacting droplet. The new researches about a drop impacting on a surface has successfully observed that the final formation of a trapped bubble of air starts from a thin film of air between the liquid and surface in the initial stage (Kolinski et al., 2012). And they also found that the fluid viscosity can affect the lift-off instability on the thin film of air (Kolinski, Mahadevan, and Rubinstein, 2014). For the elastic impactor, there is no theoretical study discussing either the formation process of central air bubble or its effect on the propagation of contact area and energy loss.

Some researches related to the adhesive contact problems of viscoelastic films have attached importance to the adhesion brought by air gap, and they studied the influencing factors of instability patterns due to the interaction between adhesive forces and elastic forces at low contact velocities (Ghatak and Chaudhury,

2003; Kendall, 1975). The research about pattern defects in high-speed reverse offset printing found that the defects are related to the air-trapping phenomenon and the air permeate into the closing crack on the PDMS film after the PDMS-glass contact (Kusaka et al., 2019).

We begin our research with the hypothesis that the air entrainment plays a significant role in the impact problem between the elastic hemi-sphere and the rigid smooth surface of a glass prism. Firstly, the experiment of an elastic hemi-sphere impacting on a rigid surface in (Dillavou, Rubinstein, and Kolinski, 2019) is reproduced and improved. To directly observe the brief initial stage of impact process with ultra-fast frame rate without sacrificing the high spatial resolution, a Total Internal Reflection (TIR) microscopy plus the Virtual Frame Technique (VFT) are adopted in the experiment, like what has been done for visualizing the impacting droplet in (Kolinski et al., 2012). For the impactor made of two types of duplication silicone, the propagation process of contact fronts under different impact velocities are recorded in the Compressed Frame Stack (CFS). Then millions of virtual frames are obtained to extract the location of contact fronts at each moment. The formation of air defects or central air bubble as well as their interaction with the impactor will be observed and analyzed.

Chapter 2

Experimental Set-up Building and Methods

In our experiment of an elastic hemi-sphere impacting on a rigid surface, one rectangular side of prism covered by an optically smooth thin glass is used as the impacted surface. The surface is illuminated by a collimated light at a specific angle in Total Internal Reflection (TIR). Because the elastic impactor can absorb the light, pixels sampling the contact area transit from white to black upon impacting. The reflected light passes through a long working-distance microscope objective and enters the Camera ORCA-Flash 4.0 V3 with 16-bit CMOS sensor. This camera provides high resolution (4.0 megapixels) and high frame rate (40 fps) by use of USB 3.0 interface. The 14.2mm-diameter elastic hemi-sphere is made by two types of duplication silicone with different Young's modulus (E) and Poisson's ratio (ν) (Elite Double 8, E =250 kPa, $\nu \approx 0.5$; Elite Double 32, E =1.1 MPa, $\nu \approx 0.5$). We control the pressure of an air gun which could speed up the elastic solid to achieve different impact velocities(2m/s, 2.5m/s, 3.5m/s, 4.5m/s, 5.5m/s). The exposure time of camera is set to 1 ms, which covers the light pulse of LED ($250 - 500$ um).
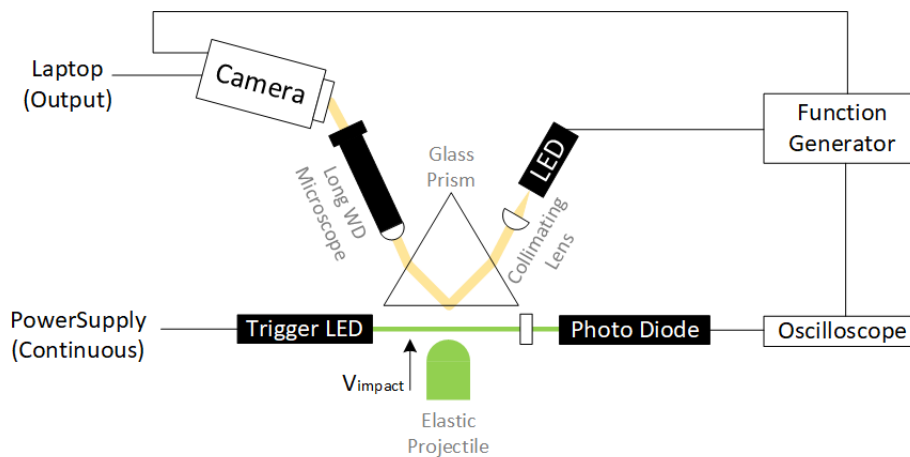

FIGURE 2.1: Schematic diagram of experimental set-up. An elastic projectile is launched from a pneumatic cannon (not shown) toward a rigid glass surface at different velocities of impact. The projectile crosses the light path sent from the trigger LED to the photo diode to trigger the oscilloscope. The function generator receives the signal from oscilloscope to trigger the camera exposure and the LED light with delay respectively.

As shown in figure 2.1, when the elastic solid crosses the light path of the trigger LED, the photo diode detects the decrease of light intensity. Then the oscilloscope receives a falling edge and sends a rising edge as an input electrical signal to the

function generator. The function generator triggers the camera and LED with different signals at different time. The impact process occurs during the light pulse of LED. Finally, we would get a blurry image, which is actually a Compressed Frame Stack (CFS) including the information of millions of virtual frames of the impact process. The most important experimental methods are explained in the following sections.

2.1   Time Control

It should be guaranteed that the impact process occurs during the light pulse of LED, which ensures that the whole impact process is captured in the Compressed Frame Stack (CFS). The following four requirements have more detailed explanations for this.

- The function generator should trigger the camera earlier than it triggers the LED, which means the time delay in the trigger signal of camera is shorter. ($\delta_{camera} < \delta_{LED}, \delta_{LED} - \delta_{camera} = 200\mu s$)

- The length of pulse light should be covered by the exposure time of camera. ($\Delta t_{LED} < \Delta t_{camera} - 200\mu s$).

- It would be better if the LED can start shining at the exact time when the impact process begins. If it is too difficult, the LED can only start a little bit earlier than that time, but not later than it. ($t^0_{LED} \leq t^0_{impact}$)

- The LED must end shining before the relative velocity of the impactor and surface becomes zero. (the end of first phase of impact process) ($t^1_{LED} < t^1_{impact}$)

The figure 2.2 presents the time diagram of the setup. However, it is very difficult to catch the moment manually when the impact process begins. If the air pressure is fixed and the length of air gun is certain, the acceleration and the distance of the elastic solid become invariant parameters. So the impact velocity should keep the same value in the repetitions of one experiment. The trigger delays of the camera and LED could be set with the reference of the beginning time of impact process. But the difference of beginning time can vary from hundreds of microseconds to several milliseconds. This is mainly due to the fact that the air gun may yaw or pitch when the impactor accelerates through it and impact direction is not vertical to the prism surface, also because the air valve is not stable and the small change in air pressure has a big effect on the impact velocity. Therefore, we have to use electronic spirit level to make sure that the orientation of air gun is at least horizontal before the experiments, which makes the difference of beginning time stable in the range of $100 - 200\mu s$. Besides, by use of a high-speed camera, we could film the impact process from the side at $10KHz$ with a resolution of 1280×480 pixels with a total of 0.6 megapixels. So we could almost find the beginning time of the impact process.

2.2   Prism Support

During the impact process, we should keep the prism surface still. Because the vibration of surface will definitely cause the non-monotonic change of intensity in the frames of impact process. But the binary and monotonic criteria are required for the
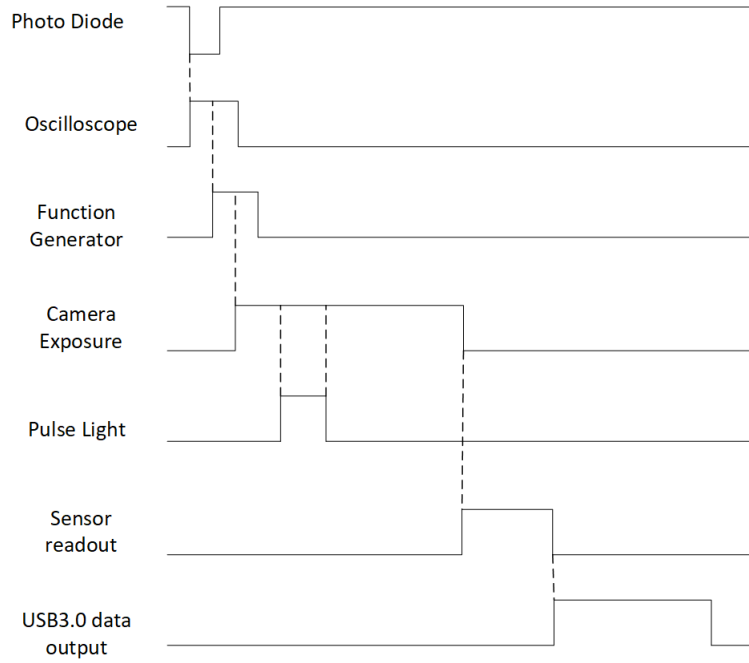
FIGURE 2.2: Time diagram. The experimental control for the relative duration and phase of each signal. The photo diode detects the intensity decrease and sends a falling edge as the input of oscilloscope, which later uses a rising edge to trigger the function generator. The function generator firstly sends a rising edge to trigger the camera exposure and then the pulse light is also triggered by function generator during the exposure time of camera. The end of camera exposure triggers the sensor readout. Finally a falling edge from the sensor readout triggers the USB3.0 data output.

use of Virtual Frame Technique (VFT). Thus, the stability of the prism surface is significantly important. To prevent the prism surface from vibration during the impact process, a heavy prism support is designed and fabricated with the metal material (Alu.Alplan). The prism support consists of two main parts - pillar and board, the 3d models of which can be observed in figure 2.3(a) and 2.3(b). The assembled support is installed on the optical board, and the prism is fixed on the support pillar by two small brides, as described in figure 2.3(c). All the connections are bolted, which guarantees the stability of the prism surface. And the Appendix A gives the technical drawings of the support pillar, board and bride.

2.3 Frustrated Total Internal Reflection(FTIR)

The quantitative Frustrated Total Internal Reflection (FTIR) technique can measure the thickness of the air film between the impacting droplet and smooth surface based on the reflected intensity (Shirota et al., 2017). However, we only use the imaging method in FTIR to image the contact interface between the impactor and the prism surface without measuring the thickness of air film. The surface is illuminated by a collimated light at an angle of incidence, which is larger than the critical angle of TIR on prism-to-air interface, but smaller than the critical angle of TIR on prism-to-silicone interface. Outside the contact area, the light from LED is totally internally reflected on the prism-to-air interface. Inside the contact area, the light from LED is partially absorbed by the elastic solid on the prism-to-silicone interface. The contact

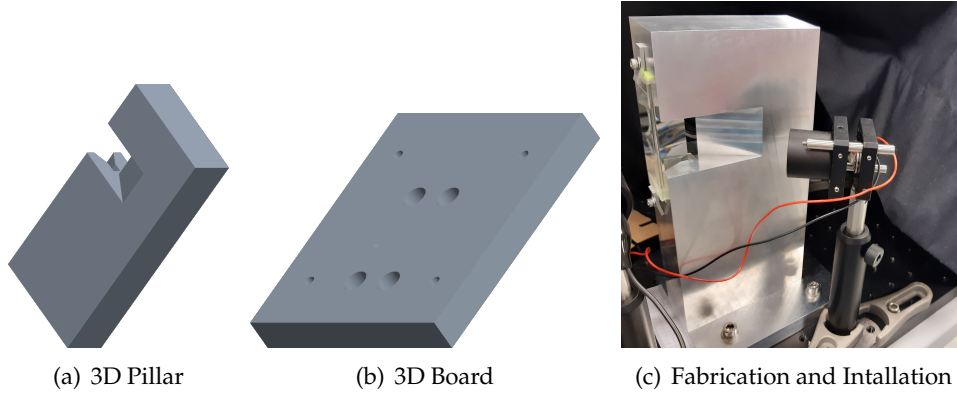(a) 3D Pillar   (b) 3D Board   (c) Fabrication and Intallation

FIGURE 2.3: Prism support. The support is designed with the aim of preventing the vibration of prism brought by the high-velocity impactor. It is composed of two main parts - pillar and board. The assembled support is installed on the optical board, and the prism is fixed on the support pillar by two small brides. (a)3D model of pillar (b)3D model of board (c)Fabrication and installation of prism support

area can present an obvious black region in the white background. As seen in figure 2.4, at the angle of incidence in FTIR (ϕ_1), the silicone impactor (n3=1.4) can absorb part of the light sent from the prism glass (n1=1.52), but the air with low refractive index (n2=1.0003) does not.
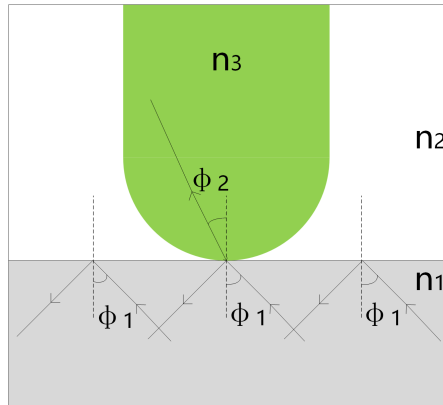

FIGURE 2.4: Frustrated Total Internal Reflection (FTIR) technique is used in this experiment to image the contact interface between the solid impactor and the prism surface without measuring the thickness of air film. At the angle of incidence in FTIR (ϕ_1), the silicone impactor (n3=1.4) can absorb part of the light sent from the prism glass (n1=1.52), but the air with low refractive index (n2=1.0003) does not. The refraction angle is (ϕ_2).

The working conditions of FTIR technique are as follows (Shirota et al., 2017),

- The refractive indexes of first and third media are larger than that of second medium $n1, n3 > n2$

- The angle of incidence ϕ_1 should be beyond the critical angle $\phi_1 > sin^{-1}(n2/n1)$.

- The light should be able to propagate through the silicone solid $\phi_1 < sin^{-1}(n3/n1)$

Finally, we obtain the working range of angle of incidence $42° < \phi_1 < 68°$ for FTIR. Note that the relationship between intensity and film thickness developed by quantitative FTIR does not work in our case because the integrated light intensity in the Compressed Frame Stack could not give the absolute intensity values.

2.4 Scheimpflug Principle

In our initial set-up, the fingerprint image shows that only a small region of subject plane is in focus, as demonstrated in figure 2.5(c). This is because the lens plane is parallel to the image plane but the lens plane is inclined at $60°$ to the subject plane, as illustrated in figure 2.5(a). According to Scheimpflug Principle (Scheimpflug, 1904; Merklinger, 1996), only by intersecting the three planes at the same line can we bring the subject plane completely in focus. Therefore, we make the prism remains still and keep the subject plane horizontal, tune the place and orientation of microscope object and camera to make the three planes intersect at the same line, as stated in figure 2.5(b). At last we achieve a sharper fingerprint image with almost the whole region in focus, as can be seen in figure 2.5(d).
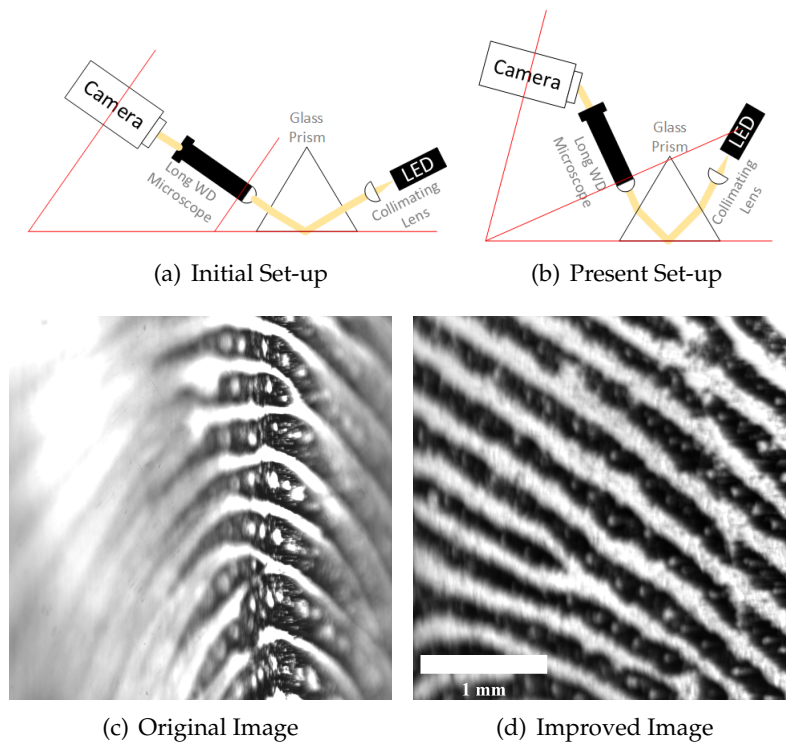

(a) Initial Set-up

(b) Present Set-up

(c) Original Image

(d) Improved Image

FIGURE 2.5: Scheimpflug Principle. (a) Initial set-up. The lens plane is parallel to the image plane but inclined at $60°$ to the subject plane. (b) The original fingerprint image only shows a small region of subject plane in focus. (c) Present set-up. Intersecting the three planes at the same line according to Scheimpflug Principle. (d) The improved fingerprint image shows that the subject plane is brought almost completely in focus.

2.5　Image Processing

The figure 2.6 presents the original CFS image and background image of one experiment. The length of pulse light is $500\mu s$, and the elastic hemi-sphere is made by Elite Double 8. The impact velocity and return velocity are $2.44m/s$ and $1.85m/s$ respectively, which are measured by the high-speed camera on the side, as indicated in figure 2.7. The impact velocity is measured over 312 pixels between Frame 96 and Frame 146 before the impact. The return velocity is measured over 237 pixels between Frame 283 and Frame 333 after the impact. The pixel size calculated based on hemi-shpere size (D=14.2mm, pixels=363) is $39.12\mu m/pixel$. The impact process between Frame 283 and Frame 290 is recorded by the high-speed camera at 10KHz with the resolution of 1280×480 pixels, as can be seen in figure 2.8. The light pulse starts before the impact and ends before the relative velocity of the impactor and surface becomes zero. Therefore, the intensity change reflected in CFS image is ensured to be monotonic and binary.
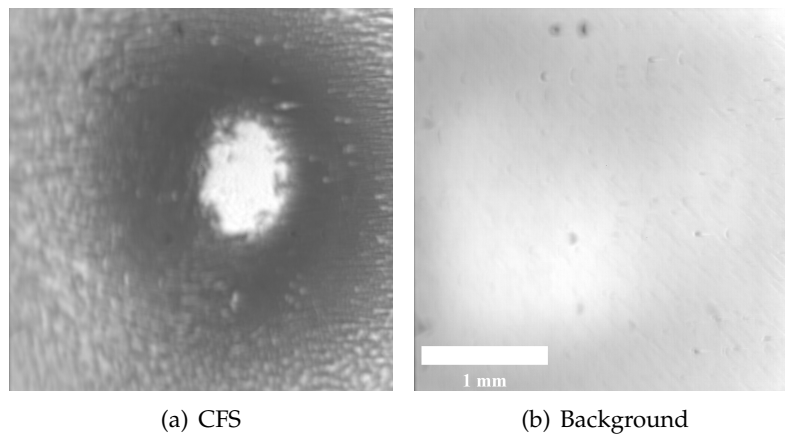

| (a) CFS | (b) Background |

FIGURE 2.6: (a) Compressed Frame Stack(CFS) (b) Background image. Pulse Length $500\mu s$, Resolution 2048×2048 pixels, Solid Material Elite Double 8, Impact Velocity $2.44m/s$
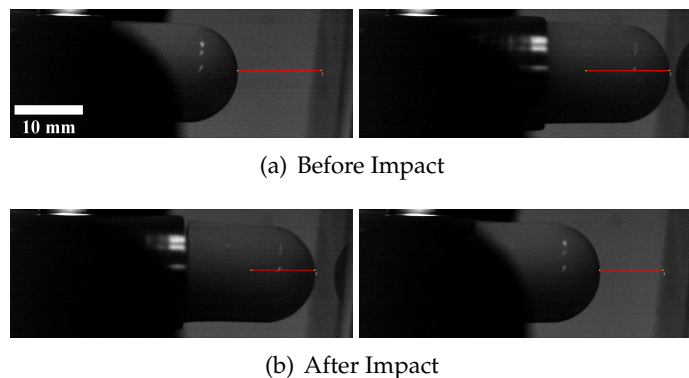

(a) Before Impact

(b) After Impact

FIGURE 2.7: Velocity measurement at 10KHz with the resolution of 1280×480 pixels, pixel size $39.12\mu m/pixel$. (a) Impact velocity $2.44m/s$ measured before impact (average velocity over 312 pixels between Frame 96 and Frame 146). (b) Return velocity $1.85m/s$ measured after impact (average velocity over 237 pixels between Frame 283 and Frame 333).
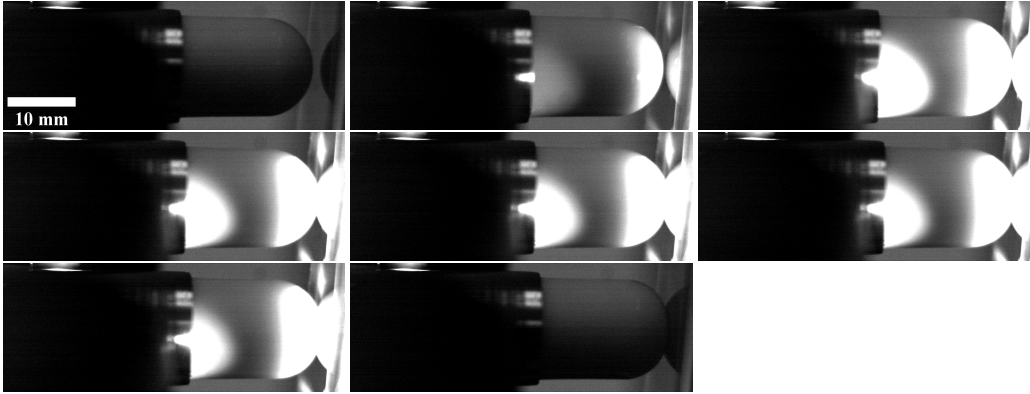
FIGURE 2.8: Initial stage of impact process between Frame 283 and Frame 290, recorded at 10KHz with the resolution of 1280 × 480 pixels. The light pulse starts before contact and ends before the relative velocity of the impactor and surface becomes zero. The intensity change reflected in CFS image is ensured to be monotonic and binary.

2.5.1 Intensity Normalization

Firstly, each CFS should subtract the background to improve the signal-to-noise ratio by dividing I(x, y, t) by I(x, y, 0). Then all the resultant intensity values are normalized to the range of 0-1.

$$I_{division} = \frac{I(x,y,t)}{I(x,y,0)} \tag{2.1}$$

$$I_{max} = MAX(I_{division}) \tag{2.2}$$

$$I_{min} = MIN(I_{division}) \tag{2.3}$$

$$I_{normal} = \frac{I_{division} - I_{min}}{I_{max} - I_{min}} \tag{2.4}$$

2.5.2 Image Transformation

The figure 2.9 illustrates the optical path in the experimental system, which could lead to the horizontal deformation of contact area. DX and DX' are the width of contact area on the subject plane and on the image plane respectively. α_c is the angle of camera inclined to the subject plane. α_1 is the angle of incidence on the air-to-prism interface. α_2 is the angle of incidence in FTIR.

According to the optical path, we could derive the relationship between the deformation ratio DX'/DX and the angle of incidence in FTIR α_2, as indicated in equation 2.10. As you can see in figure 2.10, a more direct representation of the relationship is shown. The measured aspect ratio (dx/dy) is ratio of the measured horizontal unit length and the measured vertical unit length with the help of USAF Resolving Power Test Target 1951. Because there is only horizontal deformation (no vertical deformation) in the CFS, the deformation ratio (DX'/DX) equals to the measured aspect ratio (dx/dy).

$$\frac{DX'}{DX} = \frac{cos(\alpha_2)cos(\alpha_4)}{cos(\alpha_3)cos(\alpha_5)} \tag{2.5}$$

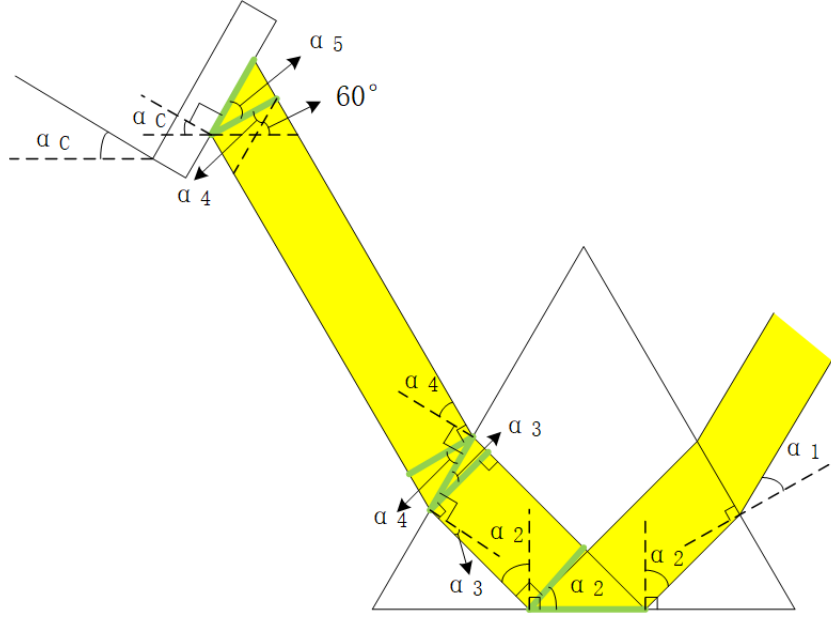$$\alpha_3 = 60° - \alpha_2 \tag{2.6}$$

FIGURE 2.9: Optical path in the experimental system. The yellow color represents the optical path. The 4 angles presented with green lines are related to the 4 transformations between the subject plane and the image plane. α_1 is the angle of incidence on the air-to-prism interface. α_2 is the angle of incidence in FTIR. α_3 is the angel of incidence on the prism-to-air interface. α_4 is the angel of refraction on the prism-to-air interface. α_5 is the angle between the sensor plane and the lens plane. α_c is the angle of camera inclined to the subject plane.

$$\alpha_5 = \alpha_4 + 30° - \alpha_c \tag{2.7}$$

$$n_{air} \cdot sin(\alpha_1) = n_{prism} \cdot sin(60° - \alpha_2) \tag{2.8}$$

$$n_{air} \cdot sin(\alpha_4) = n_{prism} \cdot sin(\alpha_3) \tag{2.9}$$

$$\frac{DX'}{DX} = \frac{cos(\alpha_2)cos(sin^{-1}(\frac{n_{prism}}{n_{air}} \cdot sin(60° - \alpha_2)))}{cos(60° - \alpha_2)cos(sin^{-1}(\frac{n_{prism}}{n_{air}} \cdot sin(60° - \alpha_2)) + 30° - \alpha_c)} \tag{2.10}$$

As can be seen in figure 2.11(a), the width (w) of Element 2 in Group 2 in USAF Resolving Power Test Target 1951 is $111.36\mu m$. The average width of horizontal line (dy) has 75.33 pixels, the average width of vertical line (dx) has 62.44 pixels. Given the deformation ratio DX'/DX (dx/dy) = 0.83, we could calculate of the angle of incidence $\alpha_2 = 42.61°$ as well as $\alpha_3 = 17.39°$, $\alpha_4 = 27.01°$ and $\alpha_5 = 25.99°$. The pixel size is $w/dy = 1.48\mu m/pixel$. After four times of projective transformation, the horizontal deformation of normalized CFS on the image plane is corrected, as reflected in figure 2.11(b). Appendix B includes the Python code of image processing.

2.6 Virtual Frame Technique(VFT)

By use of Virtual Frame Technique(VFT), we can obtain millions of virtual frames in a linear time sequence throughout the impact process. The integrated light intensity $I(x, y)$ at each pixel of CFS is uniquely dependent on the transition time when the contact occurs there, as presented in equation 2.13. The earlier the contact occurs at one point, the lower I_t the corresponding pixel has. The 16-bit CMOS sensor has
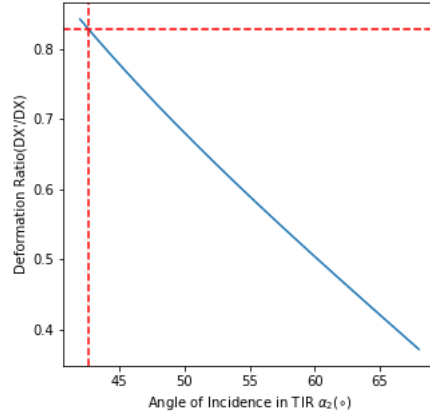
FIGURE 2.10: Relationship between the horizontal deformation ratio (DX'/DX) and the angle of incidence in FTIR (α_2), represented by the blue line. The red dotted line shows that $DX'/DX = 0.83$ corresponds to $\alpha_2 = 42.61°$. The range of α_2 in FTIR is $42° < \alpha_2 < 68°$. The deformation ratio (DX'/DX) is measured by the aspect ratio (dx/dy).

65536 grayscale values, however, only two intensity values (0 and 1) are necessary. Now the camera provides high resolution (4.0 megapixels) and high frame rate(40 fps) by use of USB 3.0 interface. By sacrificing the unnecessary bit-depth, we could dramatically increase the frame rate. Note that the working condition of VFT is that the dynamic process must be binary and monotonic.

$$I(x,y) = \frac{1}{\tau} \int_0^\pi i(x,y,t)dt \tag{2.11}$$

$$I(x,y) = 1 \cdot \frac{t_t(x,y)}{\tau} + 0 \cdot \frac{\tau - t_t(x,y)}{\tau} \tag{2.12}$$

$$t_t(x,y) = \tau \cdot I(x,y) \tag{2.13}$$

With the pulse light of $250 - 500\mu s$ length and the deconvolution process from 1 CFS to 65536 virtual frames, the impact process could be filmed at $0.13 - 0.26 GHZ$ frame rate with the resolution of 4 MPx. For example, the pulse length is $\tau = 500\mu s$, the 16-bit camera sensor has 65536 grayscale values. The theoretical maximum frame rate and smallest resolvable timestep can be calculated (ignoring noise):

$$fps_{max} = \frac{|0 - 1| \cdot 2^{16}}{500} \approx 0.13 GHz \tag{2.14}$$

$$\Delta t_{min} = 500 \times \frac{-1/65536}{0 - 1} \approx 7.63ns \tag{2.15}$$

The figure 2.12 schematically illustrate the role of VFT in analyzing the dynamic lateral propagation of the contact area on the interface. The grayscale value at each pixel in Compressed Frame Stack (CFS) uniquely maps to the transient time when the propagating fronts (outward or inward) arrive there. By thresholding the CFS image with the 10 intensity values of a linear sequence in the range of 0-1, 10 virtual frames in a linear time sequence are obtained. Appendix B includes the Python code of Virtual Frame Technique(VFT).

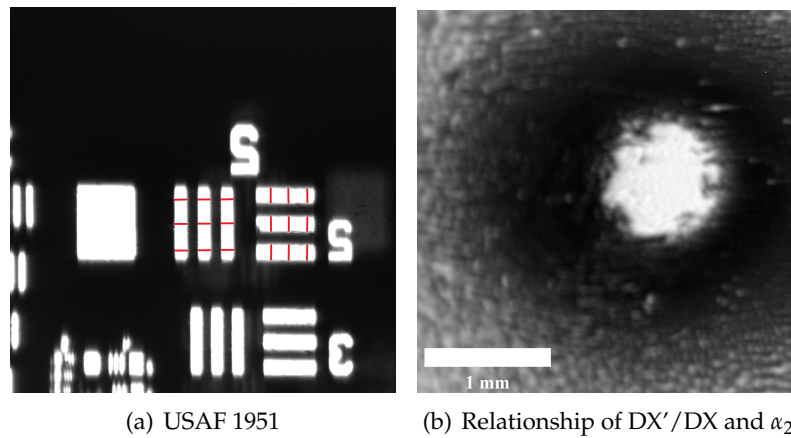(a) USAF 1951   (b) Relationship of DX′/DX and α_2

FIGURE 2.11: (a)The image of USAF 1951 Test Target used for microscopic optical resolution test. The red lines represent the measurement of the width (w) of Element 2 in Group 2 ($w = 111.36\mu s$). The average width of horizontal line (dy) has 75.33 pixels, the average width of vertical line (dx) has 62.44 pixels. The deformation ratio DX′/DX = dx/dy = 0.83. The pixel size $w/dy = 1.48\mu m/pixel$ (b)The corrected image of second experiment. The image correction includes background subtraction, normalization and projective transformation.
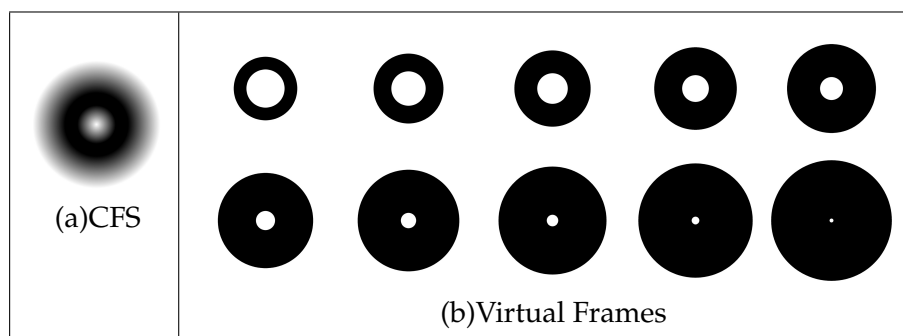

(a)CFS

(b)Virtual Frames

FIGURE 2.12: Schematical example of Virtual Frame Technique. Based on 10 intensity values between 0 and 1,(a)Compressed Frame Stack(CFS) is deconvolved to (b)10 virtual frames in a linear time sequence.

Chapter 3

Experimental Results

3.1 Compressed Frame Stack(CFS) and Virtual Frames

The table 3.1 presents the detailed information about the parameter setting and variable change of our all experiments. The impact velocities have 5 levels ($2m/s$, $2.5m/s$, $3.5m/s$, $4.5m/s$, $5.5m/s$), the solid material of hemi-sphere have two types of duplication silicone with different Young's modulus (E) and Poisson's ratio (ν) (Elite Double 8, E =250 KPa, $\nu \approx 0.5$; Elite Double 32, E =1.1 MPa, $\nu \approx 0.5$). And the pulse length are set differently according to the impact velocities. The impact process is divided to two phases by the moment when the relative velocity of the two bodies becomes zero, and the first phase has two stages (elastic deformation and plastic deformation) (Rogers and Reed, 1984).

Experiment Group	Impact Velocity	Return Velocity	Solid Material	Pulse Length	1st Phase Time	2st Phase Time
1	2.01m/s	1.76m/s	Elite Double 32	$500\mu s$	$3.3ms$	$3.5ms$
2	2.03m/s	1.62m/s	Elite Double 8	$500\mu s$	$6ms$	$8.3ms$
3	2.46m/s	2.13m/s	Elite Double 32	$500\mu s$	$3.3ms$	$3.3ms$
4	2.44m/s	1.85m/s	Elite Double 8	$500\mu s$	$5.6ms$	$8.0ms$
5	3.30m/s	2.83m/s	Elite Double 32	$450\mu s$	$3.1ms$	$3.2ms$
6	3.38m/s	2.30m/s	Elite Double 8	$450\mu s$	$4.7ms$	$6.7ms$
7	4.51m/s	3.93m/s	Elite Double 32	$350\mu s$	$2.7ms$	$3.0ms$
8	4.54m/s	2.07m/s	Elite Double 8	$350\mu s$	$3.7ms$	$5.8ms$
9	5.39m/s	4.52m/s	Elite Double 32	$250\mu s$	$3.5ms$	$2.9ms$
10	5.43m/s	2.39m/s	Elite Double 8	$250\mu s$	$3.3ms$	$6.4ms$

TABLE 3.1: The parameter setting and variable change in 10 groups of experiments. The impact velocity is the average velocity of the hemi-sphere before the impact. The return velocity is the average velocity of the hemi-sphere after the impact. The solid material of the hemi-sphere have two types of duplication silicone with different elastic modulus. The pulse length is the LED lighting time, during which the impact process is recorded in CFS. The impact process is divided to two phases by the moment when the relative velocity of the two bodies becomes zero. The phase time and velocities are calculated based on the images taken by the high-speed camera on the side.

The figure 3.1 presents the Compressed Frame Stack(CFS) of all groups. As you can see, a central air bubble exists in all the CFS images. And the groups of solid material Elite Double 8 often have a larger size of air bubble than the groups of Elite Double 32. At low impact velocities, there are a lot of air defects in the images. With
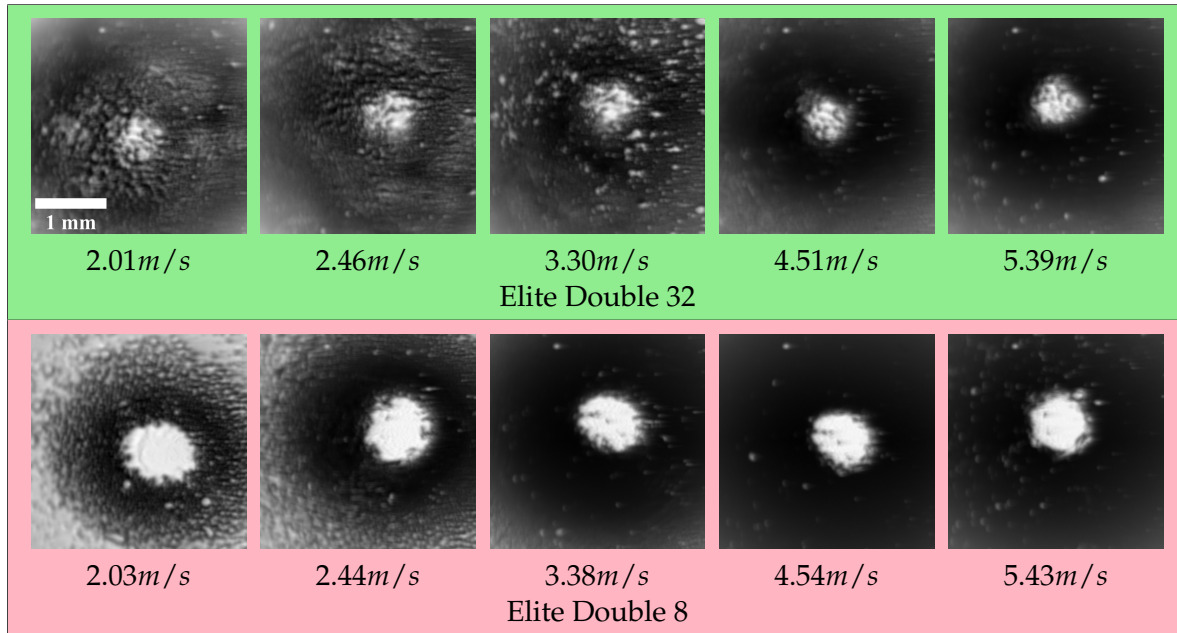
FIGURE 3.1: Compressed Frame Stack (CFS) of all groups. The images in the upper row (green background) belongs to Group 1, 3, 5, 7, 9. The solid material of hemi-shpere is Elite Double 32. The images in the lower row (pink background) belongs to Group 2, 4, 6, 8, 10. The solid material of hemi-shpere is Elite Double 8. The corresponding impact velocities are shown under the respective CFS images.

the increase of the impact velocity, the air bubble size only shrinks a little, but the air defects almost disappear in the contact region closed to the central air bubble.

All the CFS images are deconvolved to 65500 virtual frames. The figure 3.2 shows a part of the virtual frames between $13\mu s$ and $74\mu s$ of Group 3, 4, 7, 8. Appendix D has more complete virtual frames of all groups. For Group 3 and 4 at low impact velocities, the contact area appears as some isolated or connected dots and lines in the very beginning, and they rapidly joint with their neighbors and form some patchy areas. These patchy areas are unstable and changeable. There are still some air flow inside or outside these patches. These air holes are gradually filled and the patch areas are expanding with their finger-like branches, as shown in 3.3. Although the patchy areas are disperse on the surface, they are trying to form a closed ring to trap the air in the center. Of course, the air flow rate and atmospheric pressure will affect the percentage of contact area in this stage. For Group 7 and 8 at high impact velocities, the initial stage (before the closed ring is completed) is very short, which only lasts for $13\mu s - 21\mu s$ (according to Appendix D), the contact starts from larger block areas with some air defects inside it. These areas are also trying to connect with each other and form a closed ring, however, they are expanding in a more smooth shape as shown in 3.4. Actually, at the impact velocity of $3.3m/s$ (according to Appendix D), the hemi-sphere of solid material Elite Double 8 already starts to contact the surface by block areas, but that of Elite Double 32 still works by use of patchy areas.

In addition, increasing the impact velocity or decrease the solid material elastic modulus can speed up the formation and expanding of the closed ring. With the impact process going, the outer radius of the contact area propagate rapidly and covers the whole image. All the small air defects in the contact area are almost filled,
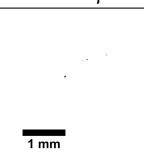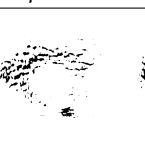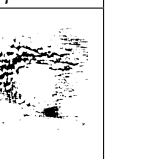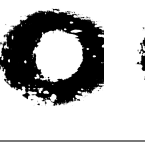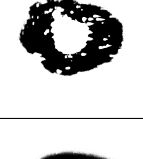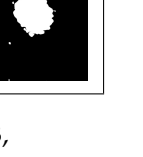
Time	$13\mu s$	$29\mu s$	$44\mu s$	$59\mu s$	$74\mu s$
Group 3 Elite Double 32 Impact velocity $2.46m/s$					
Group 4 Elite Double 8 Impact velocity $2.44m/s$					
Group 7 Elite Double 32 Impact velocity $4.51m/s$					
Group 8 Elite Double 8 Impact velocity $4.54m/s$					

FIGURE 3.2: Some virtual frames between $13\mu s$ and $74\mu s$ of Group 3, 4, 7, 8. All the CFS are deconvolved to 65500 virtual frames.

but the central air bubble only shrinks a little. In fact, from the recording of the high-speed camera, the central air bubble maintains throughout the impact process even during the second phase when the impactor rebounds from the surface.

The contact area presents several disperse patches or blocks rather than a complete ring shape in the beginning, which is different from the wetting area in the impact droplet experiment (Kolinski et al., 2012). We guess that the points on the ring area of the hemi-sphere surface could not arrive at the prism surface at the same time because of oblique impact. Although it is guaranteed by measurement that the air gun is vertical to the prism surface before the experiment, the air gun may change its orientation when the hemi-shpere accelerates through it.

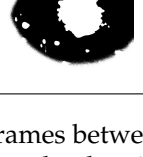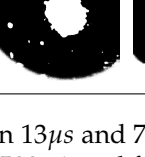(a) Group 4 - $21\mu s$ (b) Group 4 - $67\mu s$
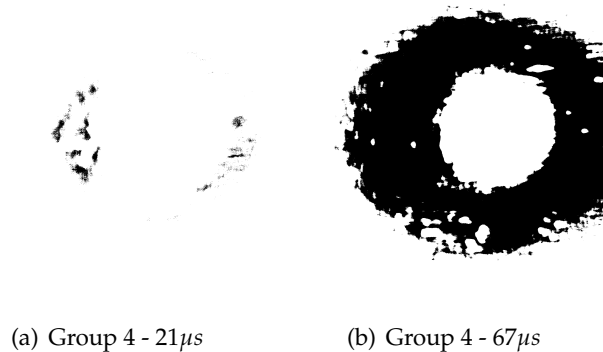
FIGURE 3.3: (a)Virtual frame of Group 4 at 21 μs presents the patchy areas in the beginning of initial stage. (b)Virtual frame of Group 4 at 67μs shows that the contact ring is expanding with finger-like branches.

The energy loss during the impact process also can be calculated based on the velocity change of the solid hemi-sphere, as you can see in figure 3.5. With the

(a) Group 8 - $8\mu s$ (b) Group 8 - $32\mu s$
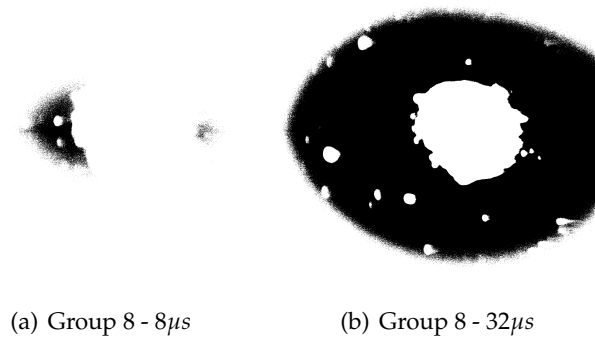
FIGURE 3.4: (a)Virtual frame of Group 8 at $8\mu s$ presents the large block areas in the very beginning of initial stage. (b)Virtual frame of Group 8 at $32\mu s$ shows that the contact ring is expanding in a smooth shape.

growth of impact velocity, the coefficient of restitution presents a decreasing tendency (energy loss is increasing). And the hemi-sphere made of Elite Double 8 with smaller Young's modulus ($E = 250KPa$) always loses more energy than the other ($E = 1.1MPa$) during the impact process. Besides, in our experiments, when the impact velocity is low ($< 0.5m/s$), the hemi-sphere probably could not rebound from the surface. And in the Group 8 experiments, brittle fracture sometimes occurs in the contact area of elastic hemi-sphere, as shown in figure 3.6. And it often occurs after repeating several experiments with the same high impact velocity ($> 5m/s$) on the same hemi-sphere made of Elite Double 8. We guess that the plastic deformation has already happened during the previous repeated experiments.
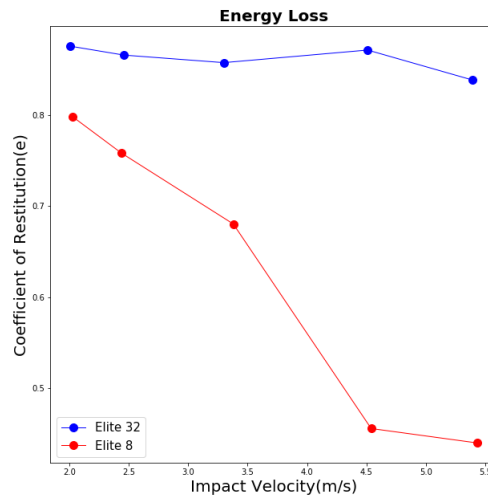
FIGURE 3.5: Energy loss is represented by the Coefficient of Restitution(e). It is the ratio of return velocity and impact velocity. The red polyline represents the solid material Elite Double 8. The blue polyline represents the solid material Elite Double 32.
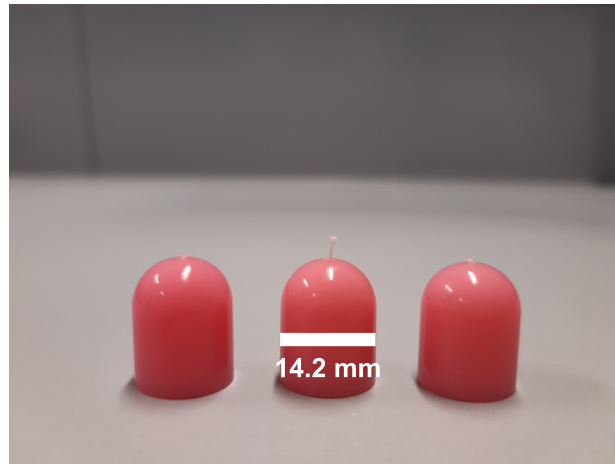
FIGURE 3.6: Three impactors made of Elite Double 8 with the brittle fracture on the contact surface. The brittle fracture often occurs after repeating several experiments with the same high impact velocity ($>$ $5m/s$).

3.2 Percentage of Contact Area

Based on the virtual binary frames obtained above, we measure the percentage of contact area (black pixels I(x,y)=0) in each frame. The figure 3.7 illustrates the change of contact area with time in our third and fourth experiments, the green square and lightgreen star represent the Group 3 (solid material Elite Double 32 with E =1.1 MPa, impact velocity 2.46/s) and Group 4 (solid material Elite Double 8 with E =250 KPa, impact speed 2.44m/s) respectively. As you can see, the percentage of contact area in Group 4 climbs rapidly in the beginning, but the growth rate presents a gradual decreasing tendency in the whole recorded time ($500\mu s$). By contrast, the increase of contact area in Group 3 experiences a longer time of gradual acceleration ($110\mu s$), and then begins to slow down. The percentage of contact area in Group 4 has been always more than that in Group 3 until 130 μs. They both reach 60% at 130 μs. And then the situation starts to reverse. With the higher growth rate, Group 3 exceeds Group 4 quickly. Finally, the percentages of contact area in the Group 4 and Group 3 both approach to their asymptotic values of 99% and 95% respectively (There are still air in the center of contact area).

The figure 3.8 compares change of contact area in our all experiments. The purple, green, blue, orange and red colors correspond to the four target impact velocities ($2m/s$, $2.5m/s$, $3.5/s$, $4.5m/s$ and $5.5m/s$) with the solid material Elite Double 32 with E = 1.1MPa , but the actual velocities have slight differences from them. The lightpurple, lightgreen, lightblue, yellow and lightred colors represent the solid material Elite Double 8 with E = 250KPa in the range of impact velocities shown above. In general, with higher and higher impact velocities, the percentage of contact area also increases more and more rapidly. At lower velocities ($2.0m/s - 3.5m/s$), the amazing increase rate of contact area in the beginning for the Elite Double 8 takes big advantage, which keeps it stay ahead the other in the initial stage. However, at higher velocities ($4.5m/s - 5.5m/s$), the advantage is not obvious anymore. The difference of the increase rate in the initial stage decrease. On the other hand, the solid material Elite Double 32 reaches its highest percentage of contact area earlier than the other at lower velocities, but the situation also reverses at higher velocities. For example, at the impact velocity of $5.5m/s$, they have almost the comparable increase
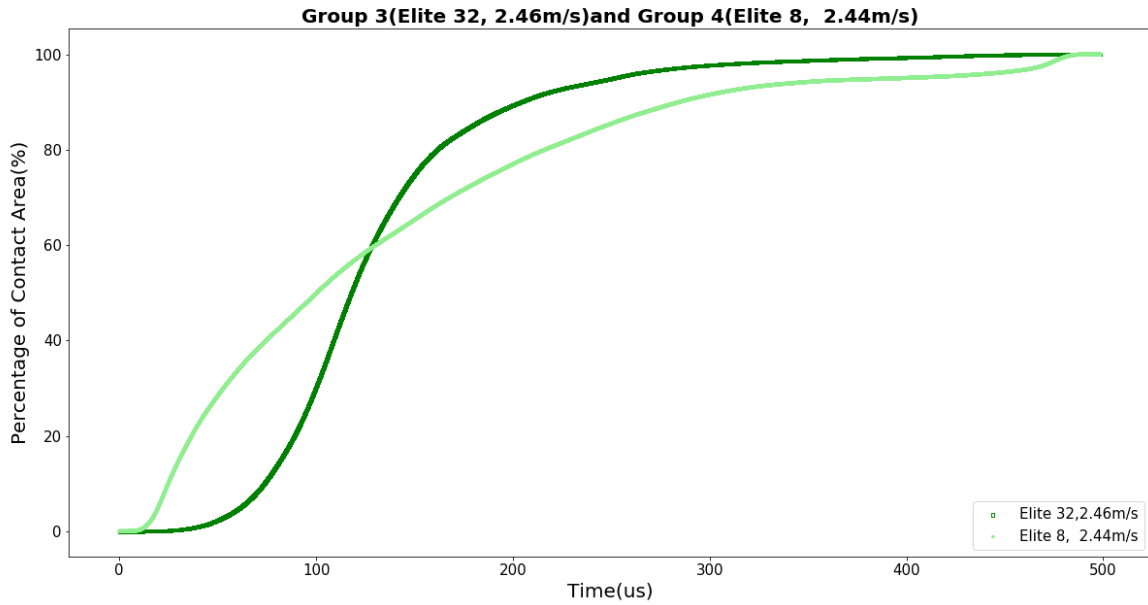
FIGURE 3.7: Percentage of Contact Area (Group 3 and Group 4) during the initial $500\mu s$ of impact process. The green square represents the Group 3 (solid material Elite Double 32 with E =1.1 MPa, impact velocity 2.46/s). The lightgreen star represents the Group 4 (solid material Elite Double 8 with E =250 KPa, impact velocity 2.44m/s).

rates in the beginning, the one that starts to decelerate earlier (solid material Elite Double 32) falls behind at last. There is still something changeless that the reachable largest contact area for the solid material Elite Double 32 is more than that for the solid material Elite Double 8 all the time, which means that there are always more air remained in the contact area of Elite Double 8.

3.3   Displacement of Contact Fronts

To extract the outward and inward contact fronts, each frame is processed by morphological operations. Firstly, the frame is resized with the scale of 0.25 and the resolution becomes 512×512 pixels. Secondly, morphological opening is applied to fill the holes inside the black contact area with an ellipse element. The size of the element change linearly with the time (from 50 to 3 pixels). Thirdly, we use the morphological closing with the ellipse element (size is fixed at 3 pixels) to remove the outlier lines or spots. The operations are demonstrated in figure 3.9. Fourthly, the frame has to be resized to the original resolution (2048×2048 pixels) before the next step. Then, the smallest convex hull is selected to cover all the contact area in the image, which is seen as the outward contact front. The average distance between all the points on the convex hull and the hull center is regarded as the radius of the outward contact front. For the inward contact front, which determines the size of the central air bubble, we look through all the contours in the image based on their hierarchy. The contour of air bubble often has parent contour(s) but it does not have any child contour, which is regarded as the first criterion. But there are still wrong closed contours detected inside the contact area. The second test criterion is to add
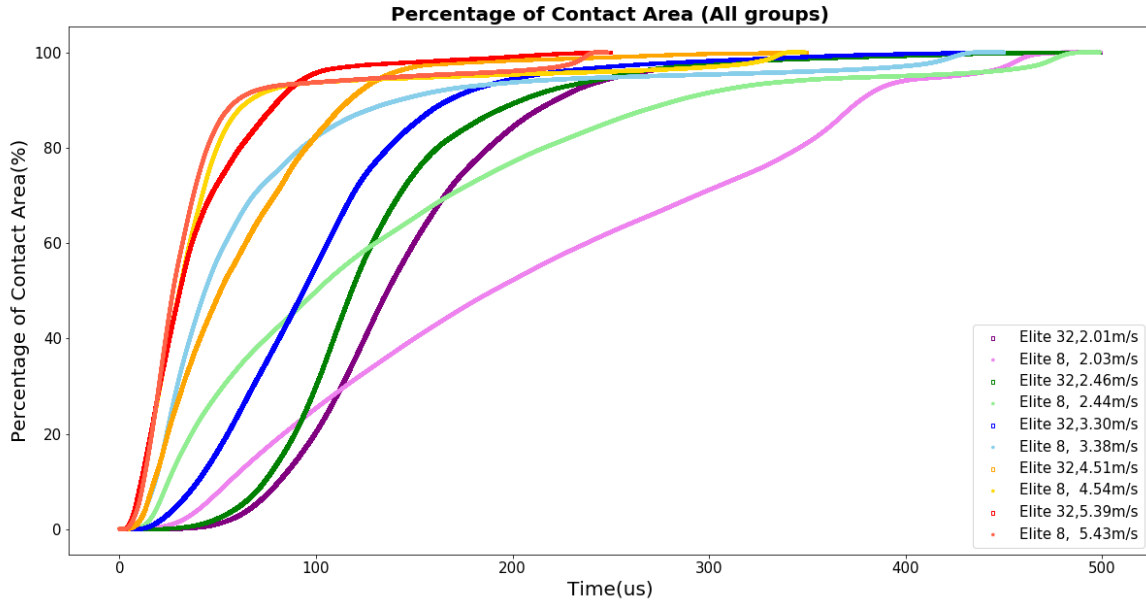
FIGURE 3.8: Percentage of Contact Area (All Groups). The purple, green, blue, orange, red colors represent the solid material Elite Double 8 with E =1.1 MPa. The lightpurple,lightgreen, lightblue, yellow, and lightred colors represent the solid material Elite Doule 8 with E =250 KPa. The purple, lightpurple, green and lightgreen show the Group 1, 2, 3 and 4 at the impact velocities of 2.01m/s, 2.03 m/s, 2.46m/s and 2.44m/s during the initial $500\mu s$ of impact process. The blue, lightblue show the Group 4 and 5 at the impact velocities of 3.30 m/s and 3.38 m/s during the initial $450\mu s$ of impact process. The orange , yellow show the Group 7 and 8 at the impact velocities of 4.51 m/s and 4.54 m/s during the initial $350\mu s$ of impact process. The red, lightred show the Group 9 and 10 at the impact velocities of 5.39 m/s and 5.43 m/s during the initial $250\mu s$ of impact process.

a limitation to the distance between the center of the newly detected contour and known center of air bubble in former frame. Even if the location of air bubble in former frame is also unknown, we can use the center of the detected convex hull (outward contact front) as a reference. As reflected in 3.10, the blue contour is the inward front, the green contour is the outward front. The two spots inside them with different colors are their respective centers.

The figure 3.11 states the distance of the contact fronts from their centers in our two experiments, also called the radius of the contact fronts. The green and lightgreen colors represent the Group 3 and 4. In Group 3, as you can see, the outward and inward contact fronts both experience a sharp radius increase (from 0 to $\sim 500\mu m$) at the initial stage, but the sharp increase of the former one always happens earlier. There are two possibilities. One is that the air bubble does not form upon impacting. The other is that the formed air bubble could not be detected successfully at that time. According to what we observe in VFT, the first possibility is more reasonable because the oblique impact can lead to the difference in contact time of the points on the hemi-sphere surface. Before the formation of the closed ring contact area, the air still can flow inside and outside the incomplete ring. Besides, it seems that the radius curve of inward and outward contact fronts of Group 3 can
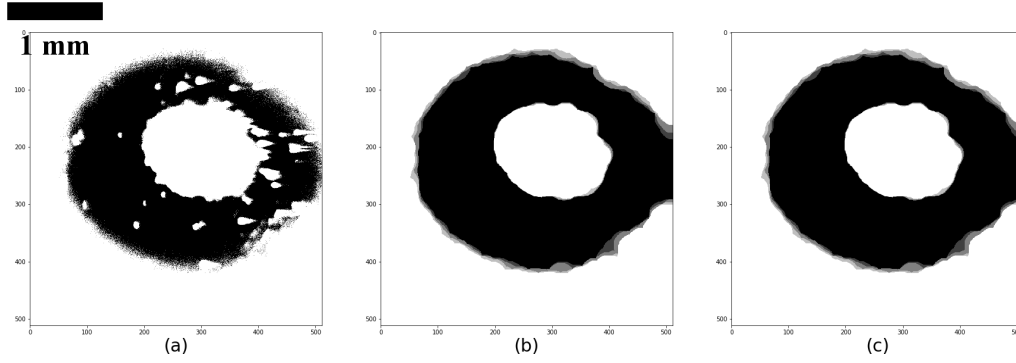
FIGURE 3.9: Morphological operations on the virtual frame at about 29μs of Group 6. (a)Resizing the virtual frame with the scale of 0.25 (b)Morphological opening with an ellipse element (size 46). (c)Morphological closing with an ellipse element (size 3).
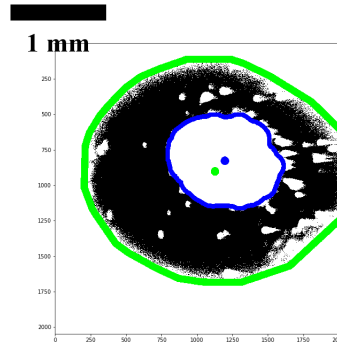

FIGURE 3.10: Outward and Inward Contact Fronts of the virtual frame at about 29μs of Group 6. The green convex hull is the outward contact front with the green spot inside as its center. The blue contour is the inward contact front with the blue spot inside as its center.

extend to meet at a point ($500\mu m < R_0 < 1000\mu m$). This actually has been proved in the experiment of droplet impact, and the point where the two meet is the radial position (R_0) at which the contact first occurs (Kolinski et al., 2012). The similar phenomenon also can be found in the Group 4, and the two curves almost meet at the point ($R_0 \approx 800\mu m$). The increase tendency in the radius of outward fronts in the two experiments are similar to that in the percentage of contact area in figure 3.7. In addition, the radius of inward contact front (central air bubble) in Group 4 (solid material Elite Double 8 with E = 250KPa) decrease slowly than that in Group 3 (solid material Elite Double 32 with E = 1.1MPa), and its asymptotic radius($\sim 400\mu m$) is also larger than the other($\sim 10\mu m$) . Both of these explain that there are more air remained inside the contact area in Group 4, which is consistent with what we find in figure 3.7.

The calculated propagating velocities of the outward and inward contact fronts in Group 3 and Group 4 are presented in figure 3.12. The green and black colors represent the two contact fronts in Group 3. The lightgreen gray colors represent the two contact fronts in Group 4. It is noticed that for each group the inward contact front forms after the formation of the outward contact front. In general, except for the initial propagating velocities, the propagating velocities of outward contact front
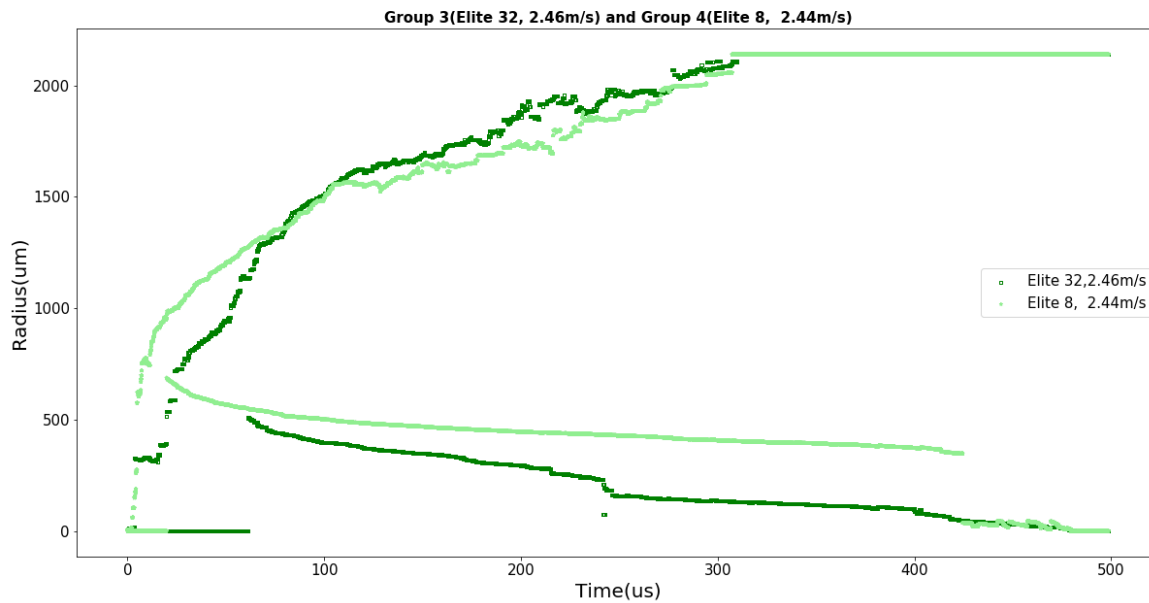
FIGURE 3.11: Distance of the Contact Fronts from the Centers (Group 3 and Group 4) during the initial $500\mu s$ of impact process. The green color represents the Group 3 (solid material Elite Doule 32 with E =1.1 MPa, impact velocity 2.46/s). The lightgreen color represents the Group 4 (solid material Elite Double 8 with E =250 KPa, impact speed 2.44m/s).

are much higher than that of inward contact front. For the outward fronts, the initial moving velocity in Group 4 ($\sim 130m/s$) is larger than that of Group 3 ($\sim 60m/s$), but later the Group 3 becomes slower than Group 3. For the inward fronts, the initial velocities are positive and the later velocities are negative. The initial inward-moving velocity in Group 4 ($\sim 140m/s$) is higher than that in Group 3($\sim 100m/s$). However, the negative inward-moving velocities in Group 3 and Group 4 have almost the same low order of magnitude ($\sim 10m/s$). So the inward front (central air bubble) often appears very abruptly in big size, but they propagates slowly.

The figure 3.13 demonstrates the change of distance of the contact fronts with time in our experiments. And the figure 3.14 and figure 3.15 give the calculated propagating velocities of outward front and inward front respectively. The distance of outward contact fronts from the center increase considerably with time, but the inward contact fronts only decrease a little. It seems that the size of central air bubble has been decided in the beginning of initial stage. The groups with high impact velocities or the impactor made of solid material Elite Double 8 (E =250 KPa) often have higher propagation speeds of contact fronts. Based on the figure 3.13, we manually find the radial positions for all the groups. The figure 3.16 shows the relationship between radial position (R_0) and impact velocity of each group. In general, the radial position decrease with the increase of impact velocity. And the impactor made of Elite Double 32 (E = 1.1 MPa) has larger radius position than that made of Elite Double 8 (E = 250 KPa). But when the impact velocity is very low (2m/s) or very high(5.5m/s), the situation is converse. And the impact velocity at 2.5m/s seems like an optimal point, where the radial position achieves the largest.
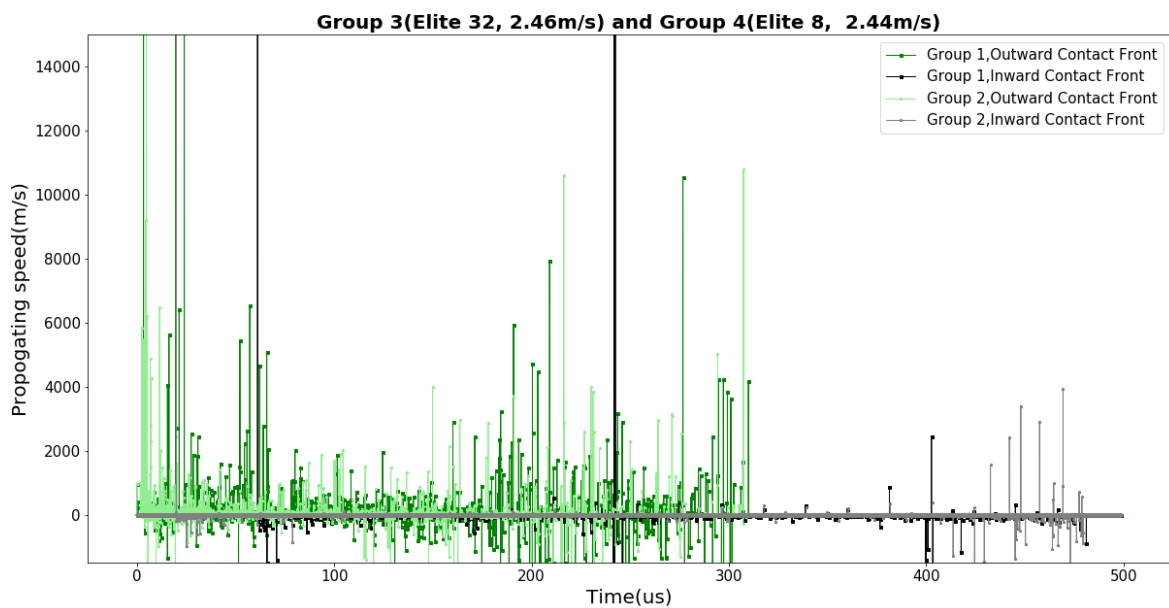
FIGURE 3.12: Propagating speeds of the contact fronts (Group 3 and Group 4) during the initial 500μs of impact process.The green and black colors represent the outward and inward contact fronts of Group 3 (solid material Elite Doule 32 with E =1.1 MPa, impact velocity 2.46/s). The lightgreen and gray colors represent the outward and inward fronts of Group 4 (solid material Elite Double 8 with E =250 KPa, impact speed 2.44m/s).
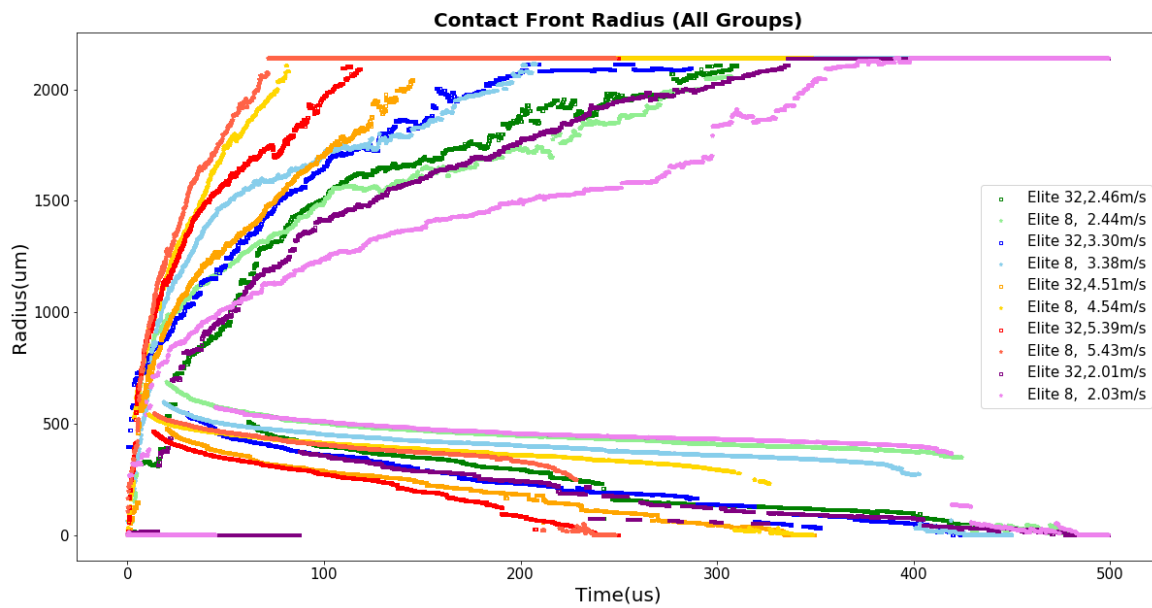
FIGURE 3.13: Distance of the Contact Fronts from the Centers (All Groups). The purple, green, blue, orange, red represent the solid material Elite Double 8 with E =1.1 MPa. The lightpurple,lightgreen, lightblue, yellow, and lightred represent the solid material Elite Double 8 with E =250 KPa. The purple, lightpurple, green and lightgreen colors show the Group 1, 2, 3 and 4 at the impact velocities of 2.01m/s, 2.03 m/s, 2.46m/s and 2.44m/s during the initial $500\mu s$ of impact process. The blue, lightblue colors show the Group 4 and 5 at the impact velocities of 3.30 m/s and 3.38 m/s during the initial $450\mu s$ of impact process. The orange, yellow colors show the Group 7 and 8 at the impact velocities of 4.51 m/s and 4.54 m/s during the initial $350\mu s$ of impact process. The red, lightred colors show the Group 9 and 10 at the impact velocities of 5.39 m/s and 5.43 m/s during the initial $250\mu s$ of impact process.

FIGURE 3.14: Propagating speeds of the outward contact fronts (All Groups). The purple, green, blue, orange, red represent the solid material Elite Double 8 with E =1.1 MPa. The lightpurple,lightgreen, lightblue, yellow, and lightred represent the solid material Elite Double 8 with E =250 KPa. The purple, lightpurple, green and lightgreen colors show the Group 1, 2, 3 and 4 at the impact velocities of 2.01m/s, 2.03 m/s, 2.46m/s and 2.44m/s during the initial $500\mu s$ of impact process. The blue, lightblue colors show the Group 4 and 5 at the impact velocities of 3.30 m/s and 3.38 m/s during the initial $450\mu s$ of impact process. The orange, yellow colors show the Group 7 and 8 at the impact velocities of 4.51 m/s and 4.54 m/s during the initial $350\mu s$ of impact process. The red, lightred colors show the Group 9 and 10 at the impact velocities of 5.39 m/s and 5.43 m/s during the initial $250\mu s$ of impact process.

FIGURE 3.15: Propagating speeds of the inward contact fronts (All Groups). The purple, green, blue, orange, red represent the solid material Elite Double 8 with E =1.1 MPa. The lightpurple,lightgreen, lightblue, yellow, and lightred represent the solid material Elite Double 8 with E =250 KPa. The purple, lightpurple, green and lightgreen colors show the Group 1, 2, 3 and 4 at the impact velocities of 2.01m/s, 2.03 m/s, 2.46m/s and 2.44m/s during the initial $500\mu s$ of impact process. The blue, lightblue colors show the Group 4 and 5 at the impact velocities of 3.30 m/s and 3.38 m/s during the initial $450\mu s$ of impact process. The orange, yellow colors show the Group 7 and 8 at the impact velocities of 4.51 m/s and 4.54 m/s during the initial $350\mu s$ of impact process. The red, lightred colors show the Group 9 and 10 at the impact velocities of 5.39 m/s and 5.43 m/s during the initial $250\mu s$ of impact process.
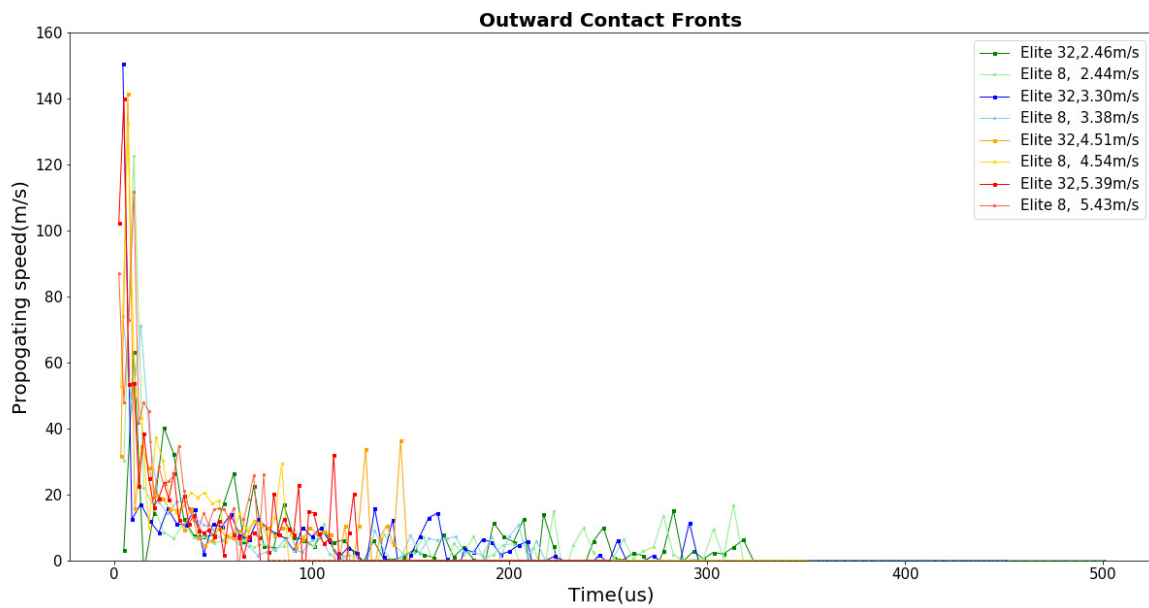
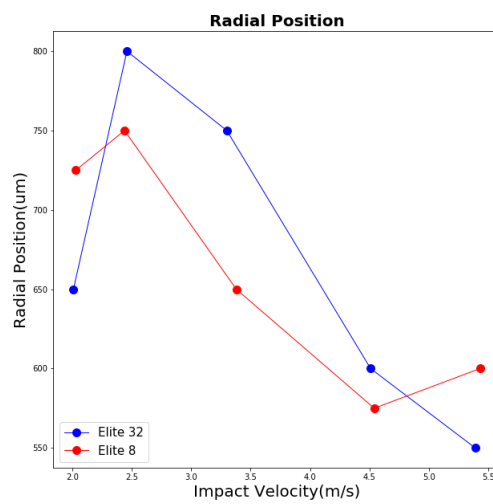FIGURE 3.16: Radial position (R_0) is the radius intersection of the outward and inward propagation contact fronts. The contact first occurs at the radial position. The red polyline represents the solid material Elite Double 8. The blue polyline represents the solid material Elite Double 32.

Chapter 4

Discussion

4.1 Stress Waves, Rubber Friction and Adhesion of the Two Bodies

The fixed prism surface and support can be regarded as a heavy rigid mass, which has more than 3 orders of magnitude higher Young's modulus than the solid hemi-sphere of duplication silicone. Assuming that there is no external or internal friction, the stress waves in the bodies are ignored and the total mass of the hemi-sphere moves as a whole at the same velocity. The deformation is restricted to the neighbouring region of the contact area and the impact process will be reversible. All the kinetic energy of the impactor can be converted to the elastic potential energy, and it is recoverable. The impactor will rebound at the same velocity as the impact velocity without energy loss. However, this quasi-static non-adhesive elastic impact is the ideal case. In fact, plastic dissipation, the propagation of elastic waves, and viscoelastic dissipation, these three interrelated mechanisms are regarded as the main cause for the energy loss during the impact process, among which the elastic waves are considered to be always present (Reed, 1985).

4.1.1 Stress Waves

The light impactor strikes the heavy prism (and support) at a high velocity, but then it slows down to zero under the compression of the prism. With the propagation of contact area, the elastic deformation of the impactor increases and the compression of the prism on the impactor goes up. When the impactor is brought to rest, the elastic deformation is the largest and the compression reaches the highest. The elastic wave fronts in a half-space by a point force will propagate from the point in a spherical shape, and this dissipation determines the minimum energy loss in any impact (Reed, 1985). According to the formula given by Reed, we could find that the fractional kinetic energy lost connects with the elastic modulus and the impact velocity $\lambda \propto K^{6/5} v^{3/5} E_2^{-3/2}$. The coefficient of restitution (e)and the parameter (K) also can be calculated by the following equations (Reed, 1985). Body 1 is the elastic impactor, and body 2 is the substrate. Therefore, increasing the impact velocity should make the coefficient of restitution decrease (fractional kinetic energy lost increases), which has been proved by our experiments. But what contradicts our results is that the low Young's modulus (E_1) of the impactor should decrease the energy loss. There should be some other reasons related to the elastic modulus of the impactor that contribute much to the energy dissipation.

$$e = (1 - \lambda)^{1/2} \tag{4.1}$$

$$K = \frac{4}{3}\left(\frac{1 - \nu_1^2}{E_1} + \frac{1 - \nu_2^2}{E_2}\right)^{-1} \tag{4.2}$$

4.1.2 Rubber Friction

The friction between the rubber and a rigid surface has two contributions - adhesion contributions (related to actual contact area) and hysteretic contributions (related to viscoelasticity) (Persson, 2001; Persson et al., 2017). The adhesion will be discussed in next section. Here the rubber friction is the internal friction that results in the hysteretic components. We have mentioned before that actually in our experiments the dynamic impact is not vertical impact, but low-angle oblique impact, which could leads to the sliding friction between the impactor and the prism surface. The internal damping of the rubber during sliding is also one of the causes for the energy dissipation, and the rubber with low elastic modulus often exhibit elastic instabilities (Persson, 2001). This could also be the reason why the coefficient of restitution becomes larger when we use the Elite Double 8 with low Young's modulus.

However, this type of viscoelactic energy dissipation is mainly due to the asperities of rough surface. The roughness of surface can have different length scales, and in our experiments the prism surface is guaranteed to be smooth both on a large scale and on a small scale, so the rubber friction may not play the main role in this case.

4.1.3 Adhesion

Van Der Waals Forces

The adhesion contribution comes from the attractive van der Waals forces between the surfaces of bodies. When applying a gentle compression to the two smooth surfaces, the weak surface forces can increase the contact area (especially for the rubber material with low elastic modulus), which could result in high sliding friction (*Rubber Friction | Research*). However, the rubber molecules do not have enough time to adjust to the substrate interaction potential, so the shear stress from the adhesion is small under large sliding speeds (Persson et al., 2017). In our experiments, the hemi-sphere impact on the surface strongly, and the impact time is very short (the first phase of impact process only lasts for $2.7ms - 6.0ms$). It is possible that there is no relative sliding between the surface and the impactor in such a short time, or even if the sliding occurs, the van der Waals forces do no have time to act.

On the other hand, we can assume that the main energy loss is due to the adhesion contribution, and it occurs in the initial stage of impact process. These can explain why the faster growth rate of the contact area percentage under the rising impact velocity also makes the energy loss increase a lot (the large contact area brings high adhesion), as shown in figure 3.8 and 3.5. However, when it comes to the comparison in the growth rates of contact area percentage for the two silicone materials, we can find that their difference in the growth rates firstly increases and then decreases with the rising impact velocity. By contrast, their difference in energy loss keeps increasing with the rising impact velocity all the time. It is not difficult to conclude that the previous assumption is wrong, maybe because the impactor loses main energy in the next stages, or the adhesion may have less contribution to the energy dissipation than we expect.

Capture of Particle

The adhesion-induced instability is regarded as the adhesive effect on the energy loss, which could cause the elastic waves (Jayadeep and Bobji, 2017). And the adhesive effect can determine the critical impact velocity for the capture of sphere. The impacting particle will probably rebound if the maximum elastic energy stored in the bodies during the impact is more than the adhesive energy between the bodies, otherwise the particle will adhere to the surface (Reed, 1985). However, the initial kinetic energy usually could not be converted to the elastic energy totally. The maximum elastic energy rely on not only the initial kinetic energy but also the different dissipation mechanisms. The energy criterion for the rebound of the impactor is shown below.

$$(Q_I - Q_P) > Q_A' \tag{4.3}$$

where Q_I, Q_P and Q_A' are the initial kinetic energy, the energy dissipated in plastic flow and the adhesive energy of second phase. Actually, in our experiments, when the impact velocity is lower than $0.5 m/s$, the hemi-sphere probably can adhere to the surface.

4.2 Effect of Air Entrainment

Compared with other reasons for the energy loss, the effect of air entrainment during the impact process has been always neglected for a long time. In our experiments, a central air bubble has been observed to be maintained in the two phases of impact process. At the end of impact process, the negative pressure of the central air bubble leads to the augment of resistance for the rebound of the impactor, which contributes to the plastic deformation and energy dissipation. In the initial stage of impact, some patchy patterns or block patterns form and gradually joint with each other with the air flowing outside or inside them. The impactor material duplication silicone is a viscoelastic material with low viscosity but high elasticity. The air film between the impactor and the prism surface has higher viscosity, compared with the impactor. For viscoelastic materials, some instability contact patterns form and grow to coalesce through adhesive forces during the impact dynamic process (Zeng et al., 2007).

4.2.1 The Adhesion-Induced Instability Patterns

Actually some instability patterns (finger-like, bubbles) at the low velocities have been studied in the contact experiments between the viscoelastic film and other plates (Ghatak and Chaudhury, 2003; Zeng et al., 2007; Kusaka et al., 2019). To find the relationship between the wavelengths of these instability patterns and the thickness film, material properties, surface roughness, velocity have been the big issue in this adhesive contact problem of viscoelastic materials. The experiments in thin confined elastic film show that the characteristic wavelengths of these instability patterns are independent of the velocity of peeling and material properties (Ghatak and Chaudhury, 2003). Our experiments at low velocities also present these instability patterns, whose size and number increase with time. We think that the system is trying to find a new balance state between the elastic forces and the adhesive forces at each moment. The balance state is transient and unstable. And the energy loss during this phase is not comparable to the energy dissipation due to the central air bubble.

However, when the hemi-sphere impacts on the surface at high velocities ($3.38m/s$ $5.43m/s$), these transient instability patterns disappear in the initial stage and the difference in outward-propagation speed of the two impactor materials decreases. Obviously,the high impact velocity accelerate the drainage of air. There are two possible reasons. Firstly, the air permeate into the impactor under the large compression. In the impact experiments of PDMS film, the air permeated into the closing crack on the PDMS film after the PDMS-glass contact and the extinction rate of the air in the film were measured (Kusaka et al., 2019). Secondly, viscoelasticity of the duplication silicone and fluid viscosity of air need enough time to interact with each other. But the high impact velocity shortens the initial stage a lot, these characteristic properties do not have time to react.

For the reason why softer Elite Double 8 can have better performance in the expansion of contact area, which means fewer air defects, larger and more patches and decreased finger-like branches, it is determined by the balance between the elastic deformation energy and the adhesion surface energy (Kendall, 1975). Here the adhesion surface energy includes not only the adhesion between the impactor and prism surface, but also the adhesion between the air and impactor, surface.

4.2.2   Central Air Bubble

The contact area has already presented an incomplete ring shape before the formation of central air bubble. We believe that if the impact is absolutely vertical to the prism surface and the surfaces are smooth enough, a closed contact ring can be observed in the beginning of initial stage. As the formation process of air bubble in (Kolinski et al., 2012), the impactor is skating on a thin air film before the contact occurs. We do not have the chance to observe it because the moment is too difficult to catch with the camera at 40 fps. The contact initially occurs when the thin air ring is broken and the transient patterns appear, and the air flow around to balance the elastic forces. Then the bubbles and channels of air are gradually filled by the solid. Some of the air run out of this area, and some is trapped inside the contact ring or other small defects.

The initial size of central air bubble is related to the material elasticity and the material properties. Actually the atmospheric pressure and surface roughness may also have effect on them. The central air bubble only shrinks a little in the next stages, compared with its initial size. Firstly, to compress the air requires a lot of forces. With the forward movement of impactor, the elastic forces go up due to the increasing elastic deformation until the impact velocity becomes zero. The compression exerted by the elastic deformation on the air bubble is limited, and it is not enough to make the air shrink a lot. Secondly, the lower elastic modulus means the solid material Elite Double 8 needs more deformation to slow down the same impact velocity to zero. It also has a larger size of air bubble, so its highest elastic forces are also more than those of the Elite Double 32.

The central air bubble has a significant effect on the energy loss in the second phase of the impact process, and the air bubble also affects the rebound and capture of the hemi-sphere. The air bubble expands to form cavities under the tensile stress, but the effect of the surface roughness on its characteristic length scale is still unknown (Ghatak and Chaudhury, 2003). In our experiments, when the elastic deformation recovery starts, the compression on the air bubble decreases and the bubble expands. When the deformation returns to zero, the air bubble already has negative pressure inside. The contact ring of impactor is still adhere to the surface because of

the pressure difference. From now on, the impactor starts elongation under the tensile stress, and the air bubble continues to expand until burst. The worst case is the brittle fracture on the hemi-sphere surface, which occurs in the conditions of high impact velocity ($> 5.3m/s$) and the hemi-sphere made of solid material Elite Double 8 ($E = 220KPa, UTS = 2MPa$). Under the high impact velocity and high elasticity of material, the impactor will have large elastic deformation and plastic deformation, the rebound resistance due to the air bubble also will increase. All of these lead to the augmentation of energy loss.

4.3 Possible Improvement

4.3.1 Impact Orientation Control

The guess about the oblique impact requires verification. The impact orientation control can help us compare the results of oblique impact and vertical impact. A precise goniometer with two rotational degrees of freedom is enough for the orientation control. Note that the base of the goniometer and the air gun has to be stable enough to sustain the vibration due to the high-velocity impactor.

4.3.2 Precise Air Flow (Impact Velocity) Control and Measurement

A large database can be helpful to the quantitative analysis in our study. Now the impact velocity varies from $2m/s$ to $5.5m/s$ with the interval of $0.5m/s$-$1m/s$. Precise air flow (impact velocity) control and measurement can improve this situation a lot. With the precise measurement and control of flow rate, the velocity could be guaranteed in each impact, which greatly increases the experimental repeatability.

4.3.3 Image Trigger

The trigger signal through photo diode and oscilloscope still has its uncertain delay. With the high-speed camera on the side, we could monitor the intensity change at a specific point on the impact path, which is very closed to the surface. The intensity change could timely trigger the LED and the camera. The image trigger not only improves the accuracy of the capture of impacting moment, but also saves a lot of time for the work.

4.3.4 Using VFT and FTIR in the Second Phase

A large amount of energy loss and the rebound of impactor both occur in the second phase of impact process. The role played by central air bubble in this phase is worth attention. To observe the change of contact area with the central air bubble inside of it, we can use VFT in the second phase. Making sure that the exposure time starts after the beginning of contact area decline could guarantee the monotonicity of intensity decrease. And transient state of the contact point still can be binary with the help of FTIR.

4.3.5 Optical Path

The light sent from LED to the camera experiences twice refraction and once reflection. The image correction from the deformed image on the camera sensor to original image on the prism surface also includes 4 transformations. It is possible to avoid

2 transformations caused by the twice refraction through the normal incidence on the sides of prism. This could decrease the errors due to the angle measurement and transformation calculations.

Chapter 5

Conclusion

In this study, an experimental apparatus was established to observe the rapid dynamic process of the contact between an elastic impactor and a rigid smooth prism surface from the contact surface and from the side. Frustrated Total Internal Reflection (FTIR), time control and the prism support ensured that the contact surface presents binary images and the propagation of contact fronts is monotonic during the light pulse, which also provided the conditions for the Virtual Frame Technique (VFT) to work. VFT played the most important role in analyzing the imaging data, which converted the 1 Compressed Frame Stack (CFS) to 65500 virtual frames without sacrificing the high resolution. An accurate original image of CFS was obtained under the guide of Schempflug principle to make the whole region of contact surface in focus. Image processing operations started from background subtraction, normalization and coordinate transformation to complete the correction for the CFS, ended with the contour seeking for the extraction of propagating contact fronts from the virtual frames.

Different from the previous studies, our research monitored and analyzed the effect of air gap between the impactor and prism surface on the impact process. The most interesting phenomenon in the experiments was that an air bubble was observed to be maintained in the center of contact area during the whole impact process, which has a big contribution to the energy loss in the second phase of the process. The impactor made of a softer material or with a lower impact velocity often can lead to a larger initial size of central air bubble. And this initial size only shrinks a little in the initial stage because of the large pressure inside the bubble, however, it begins to expand and has negative pressure under the tensile force in the second phase. This also explains why it prevents the impactor from rebounding. The high impact velocity can increase the pressure difference caused by the negative pressure and the resistance brought by it. With high impact velocities and low elastic modulus, the propagation of outward contact fronts also become faster because of the great decrease of air defects and the disappearance of instability patterns. The guess is that the air permeates into the tiny cracks on the impactor surface, which appear due to the high stress.

The similar phenomenon has been observed both in droplet impact and the elastic solid impact, which means that the role played by air gap in the impact problems should not be neglected. The air gap between the two solids also has its effect on stress distribution, energy loss and contact propagation. The central air bubble even can affect the impact process all the time.

In the future work, a series of improvement measures are possible for the experiments. More accurate quantitative analysis of the radial position and energy loss could be completed with more imaging data. More precise impact orientation control, air flow (impact velocity) control and time control can guarantee the high

quality of images. Besides, more researches can be done about the permeation of air in the initial stage and the performance of air bubble in the second phase.

Bibliography

Bowden, F P and D Tabor (1966). "Friction, lubrication and wear: a survey of work during the last decade". In: *British Journal of Applied Physics* 17.12, pp. 1521–1544. DOI: 10.1088/0508-3443/17/12/301. URL: https://doi.org/10.1088%2F0508-3443%2F17%2F12%2F301.

Cotsovos, D. M., N. D. Stathopoulos, and C. A. Zeris (2008). "Behavior of RC Beams Subjected to High Rates of Concentrated Loading". In: *Journal of Structural Engineering* 134.12, pp. 1839–1851. DOI: 10.1061/(ASCE)0733-9445(2008)134:12(1839).

Dillavou, S., S. M. Rubinstein, and J. M. Kolinski (2019). "The virtual frame technique: ultrafast imaging with any camera". In: *Opt. Express* 27.6, pp. 8112–8120. DOI: 10.1364/OE.27.008112. URL: http://www.opticsexpress.org/abstract.cfm?URI=oe-27-6-8112.

Ghatak, Animangsu and Manoj K. Chaudhury (2003). "Adhesion-Induced Instability Patterns in Thin Confined Elastic Film". In: *Langmuir* 19.7, pp. 2621–2631. DOI: 10.1021/la026932t. eprint: https://doi.org/10.1021/la026932t. URL: https://doi.org/10.1021/la026932t.

Jayadeep, U.B. and M.S. Bobji (2017). "Energy Loss Due to Adhesion During the Impact of Elastic Spheres". In: *Procedia Engineering* 173. Plasticity and Impact Mechanics, pp. 238 –243. ISSN: 1877-7058. DOI: https://doi.org/10.1016/j.proeng.2016.12.004. URL: http://www.sciencedirect.com/science/article/pii/S1877705816343958.

Johnson, K. L. (1985). "Dynamic effects and impact". In: *Contact Mechanics*. Cambridge University Press, 340–373. DOI: 10.1017/CBO9781139171731.012.

Kendall, K (1975). "Thin-film peeling-the elastic term". In: *Journal of Physics D: Applied Physics* 8.13, pp. 1449–1452. DOI: 10.1088/0022-3727/8/13/005. URL: https://doi.org/10.1088%2F0022-3727%2F8%2F13%2F005.

Kogut, L. and I. Etsion (Aug. 2002). "Elastic-Plastic Contact Analysis of a Sphere and a Rigid Flat ". In: *Journal of Applied Mechanics* 69.5, pp. 657–662. ISSN: 0021-8936. DOI: 10.1115/1.1490373. eprint: https://asmedigitalcollection.asme.org/appliedmechanics/article-pdf/69/5/657/5468980/657_1.pdf. URL: https://doi.org/10.1115/1.1490373.

Kolinski, John M. et al. (2012). "Skating on a Film of Air: Drops Impacting on a Surface". In: *Phys. Rev. Lett.* 108 (7), p. 074503. DOI: 10.1103/PhysRevLett.108.074503. URL: https://link.aps.org/doi/10.1103/PhysRevLett.108.074503.

Kolinski, John Martin, L. Mahadevan, and Shmuel M. Rubinstein (2014). "Lift-off instability during the impact of a drop on a solid surface." In: *Physical review letters* 112 13, p. 134501.

Kral, E., K. Komvopoulos, and David Bogy (Dec. 1993). "Elastic-Plastic Finite Element Analysis of Repeated Indentation of a Half-Space by a Rigid Sphere". In: *Journal of Applied Mechanics-transactions of The Asme - J APPL MECH* 60. DOI: 10.1115/1.2900991.

Kusaka, Yasuyuki et al. (2019). "Patterning defects in high-speed reverse offset printing: lessons from contact dynamics". In: *Journal of Micromechanics and Microengineering* 29.4, p. 045001. DOI: `10.1088/1361-6439/ab024b`. URL: `https://doi.org/10.1088%2F1361-6439%2Fab024b`.

Liu, Jianfeng et al. (2018). "Influence of layer number and air gap on the ballistic performance of multi-layered targets subjected to high velocity impact by copper EFP". In: *International Journal of Impact Engineering* 112, pp. 52 –65. ISSN: 0734-743X. DOI: `https://doi.org/10.1016/j.ijimpeng.2017.10.001`. URL: `http://www.sciencedirect.com/science/article/pii/S0734743X1730578X`.

Merklinger, Harold (1996). *Focusing the View Camera*. Bedford, Nova Scotia: Seaboard Printing Limited. ISBN: ISBN 0-9695025-2-4. URL: `http://www.trenholm.org/hmmerk/download.html`.

MultiscaleConsulting. *Rubber Friction | Research*. `http://www.multiscaleconsulting.com/our-research/rubber-friction`. [Online; accessed 11-January-2020].

Persson, B. N. J. et al. (2017). "Multiscale Contact Mechanics with Application to Seals and Rubber Friction on Dry and Lubricated Surfaces". In: *Designing of Elastomer Nanocomposites: From Theory to Applications*. Ed. by Klaus Werner Stöckelhuber, Amit Das, and Manfred Klüppel. Cham: Springer International Publishing, pp. 103–156. ISBN: 978-3-319-47696-4. DOI: `10.1007/12_2016_4`. URL: `https://doi.org/10.1007/12_2016_4`.

Persson, Bo (Aug. 2001). "Theory of rubber friction and contact mechanics". In: *The Journal of Chemical Physics* 115. DOI: `10.1063/1.1388626`.

Reed, J (1985). "Energy losses due to elastic wave propagation during an elastic impact". In: *Journal of Physics D: Applied Physics* 18.12, pp. 2329–2337. DOI: `10.1088/0022-3727/18/12/004`. URL: `https://doi.org/10.1088%2F0022-3727%2F18%2F12%2F004`.

Rogers, L N and J Reed (1984). "The adhesion of particles undergoing an elastic-plastic impact with a surface". In: *Journal of Physics D: Applied Physics* 17.4, pp. 677–689. DOI: `10.1088/0022-3727/17/4/007`. URL: `https://doi.org/10.1088%2F0022-3727%2F17%2F4%2F007`.

Scheimpflug, Theodor (1904). "Improved Method and Apparatus for the Systematic Alteration or Distortion of Plane Pictures and Images by Means of Lenses and Mirrors for Photography and for other purposes". Pat. 1196. URL: `http://www.trenholm.org/hmmerk/TSBP.pdf`.

Shirota, Minori et al. (2017). "Measuring thin films using quantitative frustrated total internal reflection (FTIR)". In: *The European Physical Journal E* 40.5, p. 54. ISSN: 1292-895X. DOI: `10.1140/epje/i2017-11542-4`. URL: `https://doi.org/10.1140/epje/i2017-11542-4`.

Zeng, Hongbo et al. (2007). "Transient Surface Patterns and Instabilities at Adhesive Junctions of Viscoelastic Films". In: *Macromolecules* 40.23, pp. 8409–8422. DOI: `10.1021/ma0712807`. eprint: `https://doi.org/10.1021/ma0712807`. URL: `https://doi.org/10.1021/ma0712807`.

Appendix A
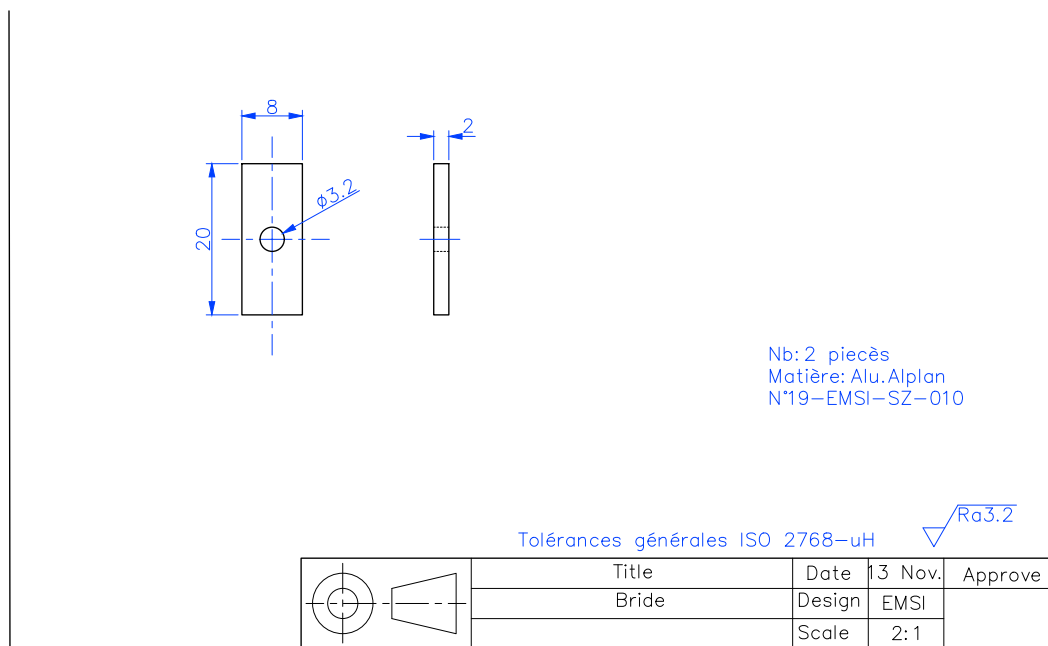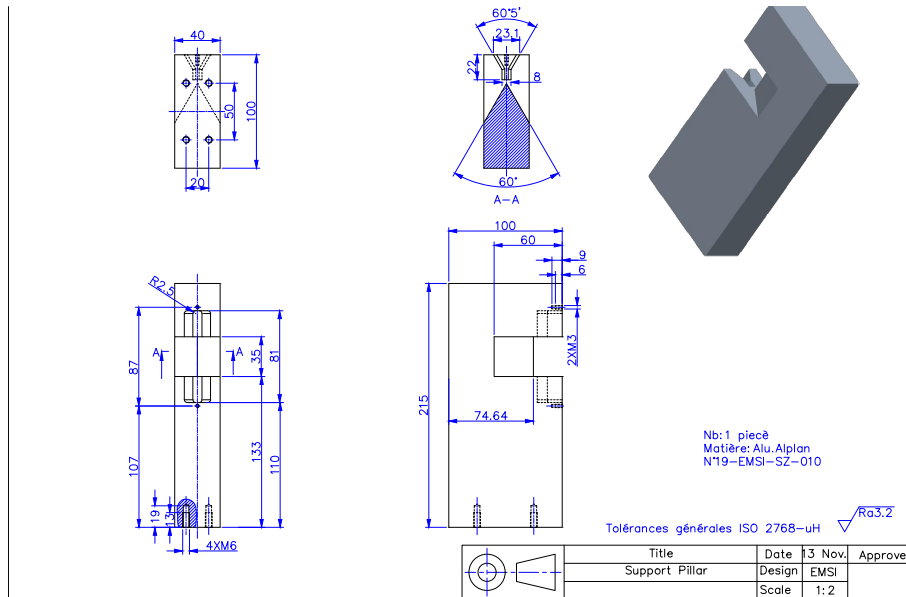
Prism Support
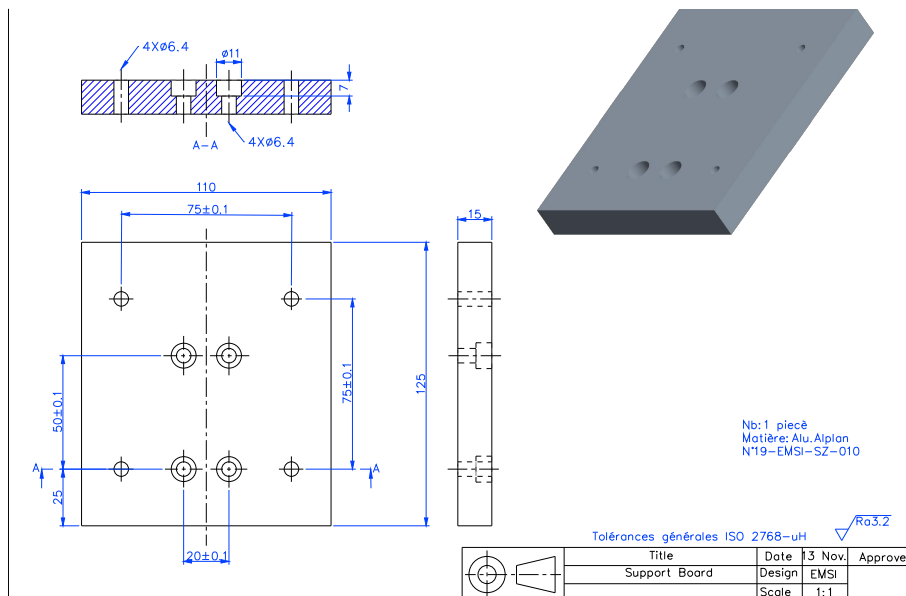

FIGURE A.1: Bride

FIGURE A.2: Support Pillar

FIGURE A.3: Support Board

Appendix B

Python

B.1 Virtual Frame Technique

```python
#!/usr/bin/env python
# coding: utf-8

# In[ ]:


"""Deconvolution from one stack to virtual frames"""

# columns = 5
# rows = 3
# fig = plt.figure(figsize=(20, 8))

# Number of virtual frames
num_frames = 65500

# Image array
frame_array = []

# path to save Virtual Frames
pathout = 'E:/Siqi/VFT_5p5_250_8'

for thresh in range(num_frames):

    # Thresholding the intensity of Compressed Frame Stack
    grascale = thresh / num_frames
    binary = img_output > grascale

    # Show the virtual frames in jupyter
    # fig.add_subplot(rows, columns, thresh)
    # plt.imshow(binary,cmap = 'gray',interpolation = 'none')

    # Change data type of virtual frame from bool to uint8 and save
    them
    binary_img = binary.astype('uint8') * 255
    cv2.imwrite(os.path.join(pathout , "%d.png"%thresh), binary_img )

    # inserting the frames into an image array
    #frame_array.append(binary_img )
```

B.2 Image Processing

```python
#!/usr/bin/env python
# coding: utf-8

# In[ ]:

```

```python
6
7  """Compressed Frame Stack background removement"""
8
9  # Load images as NumPy array
10 grat_img = skimage.io.imread('D:/Siqi/results/2_500_8.tif')
11 back_img = skimage.io.imread('D:/Siqi/results/2_500_8b.tif')
12
13 # Normalization
14 normal_img = grat_img/back_img
15
16 # Show image
17 plt.figure(figsize=(5,5))
18 plt.imshow(normal_img,cmap = 'gray',interpolation = 'none')
19
20
21 # In[ ]:
22
23
24 """Optical transfer function to obtain the angle of incidence for the
     prism"""
25
26 # refractive ratio
27 n_air=1.000293
28 n_prism=1.52
29 n = n_prism/n_air
30
31 # angle of camera
32 angle_c=23
33
34 # Measured aspect ratio (dx/dy) by USAF 1951 1X
35 dx = 62.44
36 dy = 75.33
37
38 ratio_measured = dx/dy
39 print('Measured aspect ratio(dx/dy)',ratio_measured)
40
41 # plot the change of calculated aspect ratio with the angle of
     incidence
42 x = np.linspace(42,68,num=1000)
43 f4 = np.cos(x*np.pi/180)/np.cos((60-x)*np.pi/180)*np.cos(np.arcsin(n*np
     .sin((60-x)*np.pi/180)))/np.cos(np.arcsin(n*np.sin((60-x)*np.pi
     /180))+(30-angle_c)*np.pi/180)
44 angle_1=optimize.bisect(lambda x: np.cos(x*np.pi/180)/np.cos((60-x)*np.
     pi/180)*np.cos(np.arcsin(n*np.sin((60-x)*np.pi/180)))/np.cos(np.
     arcsin(n*np.sin((60-x)*np.pi/180))+(30-angle_c)*np.pi/180)-
     ratio_measured, 25, 90)
45 angle_2=np.arcsin(n*np.sin((60-angle_1)*np.pi/180))*180/np.pi
46 print('The calculated angle of incidence from prism to air(a1>=42) ',
     angle_1)
47 print('The calculated angle of incidence from air to prism (a2<=28)',
     angle_2)
48
49 plt.figure(figsize=(5,5))
50 plt.plot(x,f4)
51 plt.xlabel(r'angle of incidence $\phi(\circ)$')
52 plt.ylabel('Measured aspect ratio(dx/dy)')
53 plt.axhline(y=ratio_measured,c='red',linestyle='dashed' )
54 plt.axvline(x=angle_1, c='red',linestyle='dashed' )
55 plt.savefig('relation.png')
56 plt.show()
57
58
59 # In[ ]:
```

```python
60
61
62  """Image transformation"""
63
64  # Reference for pixel size
65  len_sample = 111.36
66  size_pixel = len_sample/75.33
67
68  # Projective transformation
69  src_points=np.float32([[0,0],[2047,0],[0,2047],[2047,2047]])
70  dst3_points=np.float32([[2047-2047*np.cos(angle_c*np.pi/180)
        ,0],[2047,0],[2047-2047*np.cos(angle_c*np.pi/180)
        ,2047],[2047,2047]])
71  dst2_points=np.float32([[0,0],[2047/np.cos(angle_2*np.pi/180)
        ,0],[0,2047],[2047/np.cos(angle_2*np.pi/180),2047]])
72  dst1_points=np.float32([[2047-2047*np.cos((60-angle_1)*np.pi/180)
        ,0],[2047,0],[2047-2047*np.cos((60-angle_1)*np.pi/180)
        ,2047],[2047,2047]])
73  dst0_points=np.float32([[2047-2047/np.cos(angle_1*np.pi/180)
        ,0],[2047,0],[2047-2047/np.cos(angle_1*np.pi/180)
        ,2047],[2047,2047]])
74
75  projective3_matrix=cv2.getPerspectiveTransform(src_points,dst3_points)
76  projective2_matrix=cv2.getPerspectiveTransform(src_points,dst2_points)
77  projective1_matrix=cv2.getPerspectiveTransform(src_points,dst1_points)
78  projective0_matrix=cv2.getPerspectiveTransform(src_points,dst0_points)
79
80  img3_output=cv2.warpPerspective(normal_img,projective3_matrix
        ,(2048,2048))
81  img2_output=cv2.warpPerspective(img3_output,projective2_matrix
        ,(2048,2048))
82  img1_output=cv2.warpPerspective(img2_output,projective1_matrix
        ,(2048,2048))
83  img0_output=cv2.warpPerspective(img1_output,projective0_matrix
        ,(2048,2048))
84
85  # Normalizaiton
86  Imax = img0_output.max()# Maximum intensity
87  print(Imax)
88  Imin = img0_output.min()# Minimum intensity
89  print(Imin)
90  img_output = (img0_output-Imin)/(Imax-Imin)
91
92  plt.figure(figsize=(5,5))
93  plt.imshow(img_output,cmap = 'gray',interpolation = 'none')
94
95
96  # In[ ]:
97
98
99  """Contact area, Displacement of contact fronts"""
100 import csv
101
102 area_array=[]
103 radius1_array=[]
104 radius2_array=[]
105
106 # Number of virtual frames
107 num_frames = 65500
108
109 # Image array
110 frame_array = []
111
```

```python
112  for thresh in range(num_frames):
113
114      # Thresholding
115      grascale = thresh / num_frames
116      binary = img_output > grascale
117
118      #Change data type of virtual frame from bool to uint8
119      binary_frame = binary.astype('uint8') * 255
120
121      # Percentage of Contact Area
122      area = (2048*2048-cv2.countNonZero(binary_frame))/(2048*2048)*100
123      area_array.append(area)
124
125      # Resize Image
126      normal_img = cv2.resize(binary_frame, dsize=(0, 0), fx=0.25, fy
         =0.25)
127
128      # Morphological opening:
129      s = int(50-thresh / num_frames * 47)
130      normal_img = cv2.morphologyEx(normal_img, cv2.MORPH_OPEN, cv2.
         getStructuringElement(cv2.MORPH_ELLIPSE, (s, s)))
131
132      # Morphological Closing:
133      normal_img = cv2.morphologyEx(normal_img, cv2.MORPH_OPEN, cv2.
         getStructuringElement(cv2.MORPH_ELLIPSE, (3,3)))
134
135      # Resize Image
136      normal_img = cv2.resize(normal_img, dsize=(0, 0), fx=4, fy=4)
137
138      # Convex hull - outward front
139      substract_img=cv2.subtract(255, normal_img)
140      hull = skimage.morphology.convex_hull_image(substract_img)
141      convex_hull =hull.astype('uint8') * 255
142      _,convex_contour,_= cv2.findContours(convex_hull,cv2.RETR_TREE, cv2
         .CHAIN_APPROX_SIMPLE)
143      holes=[]
144
145      if len(convex_contour)<1:
146          radius1=0
147      else:
148          M1 = cv2.moments(convex_contour[0])
149          Cx1 = int(M1['m10']/M1['m00'])
150          Cy1 = int(M1['m01']/M1['m00'])
151          dist1 = np.square(convex_contour[0][:,0]-(Cx1,Cy1))
152          radius1 = np.sqrt(np.mean(dist1[:,0]+dist1[:,1]))
153
154          # Find contour - inward front
155          Cx2=Cx1
156          Cy2=Cy1
157          _,contours,hierarchy= cv2.findContours(substract_img,cv2.
             RETR_CCOMP, cv2.CHAIN_APPROX_NONE)
158
159          for i in range(len(contours)):
160              if hierarchy[0][i][2] < 0 and hierarchy[0][i][3] > -1:
161                  M2 = cv2.moments(contours[i])
162                  Cx2_new = int(M2['m10']/M2['m00'])
163                  Cy2_new = int(M2['m01']/M2['m00'])
164                  dist_c =np.sqrt(((Cx2_new-Cx2)**2+(Cy2_new-Cy2)**2)/2)
165                  if dist_c <230:
166                      Cx2=Cx2_new
167                      Cy2=Cy2_new
168                      holes.append(contours[i])
169                      break
```

```
170
171     if len(holes)<1:
172         radius2=0
173     else:
174         dist2 = np.square(holes[0][:,0]-(Cx2,Cy2))
175         radius2 = np.sqrt(np.mean(dist2[:,0]+dist2[:,1]))
176
177     radius1_array.append(radius1)
178     radius2_array.append(radius2)
```

Appendix C
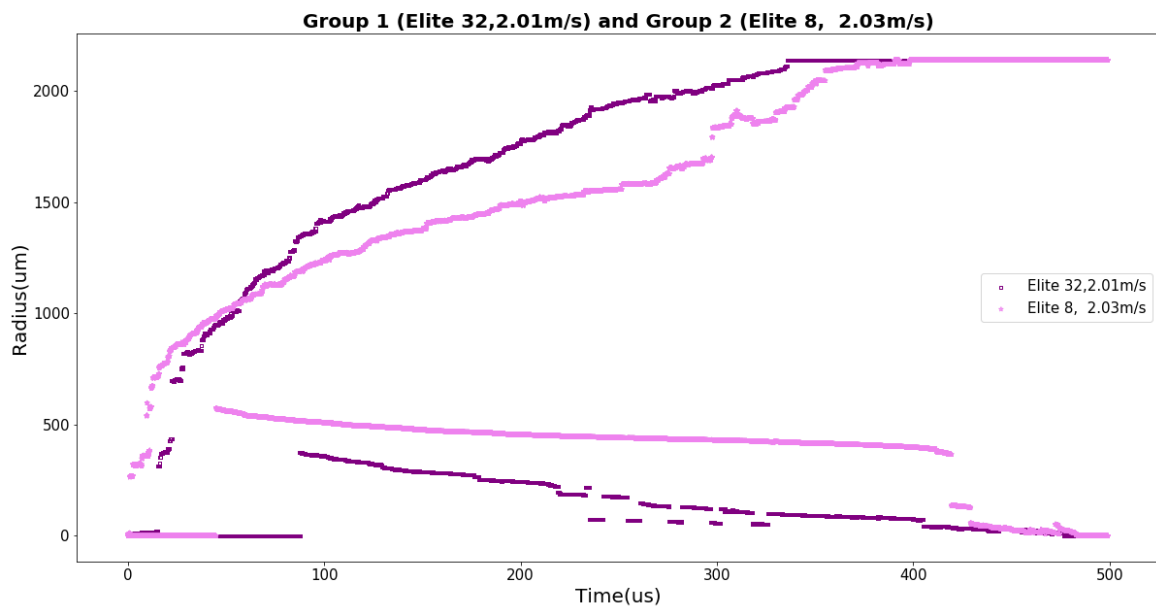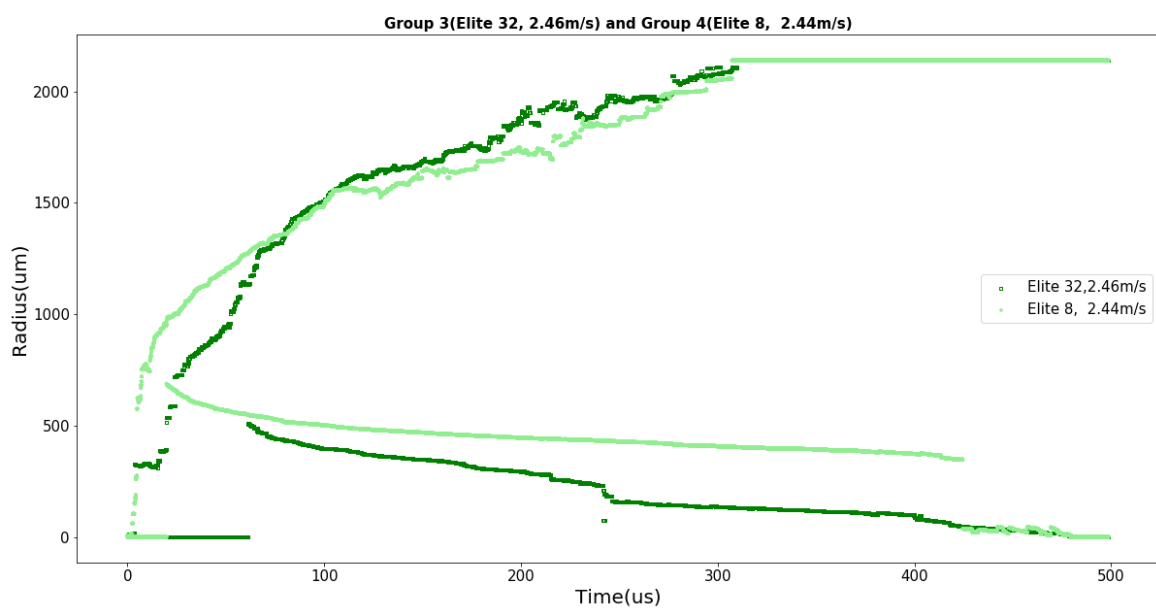
Propagation of Contact Fronts

FIGURE C.1: Distance of the Contact Fronts from the Centers (Group 1 and Group 2) during the initial $500\mu s$ of impact process. The purple color represents the Group 1 of Elite Doule 32 (E =1.1MPa) and impact velocity 2.01m/s. The lightpurple color represents the Group 2 of Elite Double 8 (E =250 KPa) and impact speed 2.03m/s.
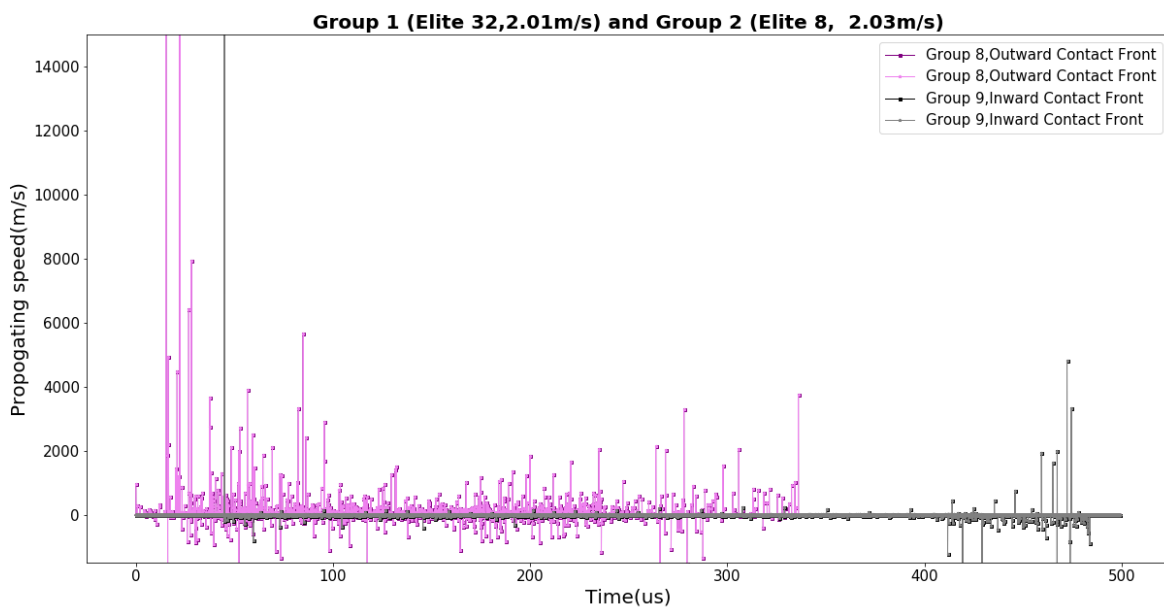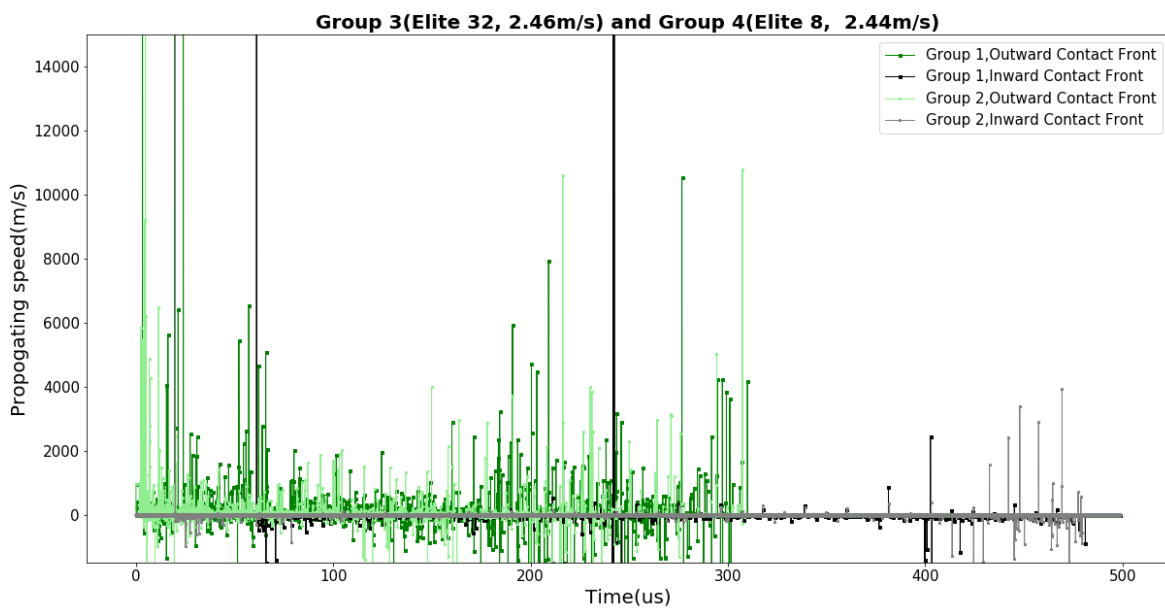
FIGURE C.2: Propagating speeds of the outward contact fronts (Group 1 and Group 2) during the initial $500\mu s$ of impact process. The purple and black colors represent the outward and inward contact fronts in Group 1 of Elite Doule 32 (E =1.1 MPa) and impact velocity 2.01/s. The lightpurple and gray colors represent the outward and inward fronts in Group 2 of Elite Double 8 (E =250 KPa) and impact speed 2.03m/s.
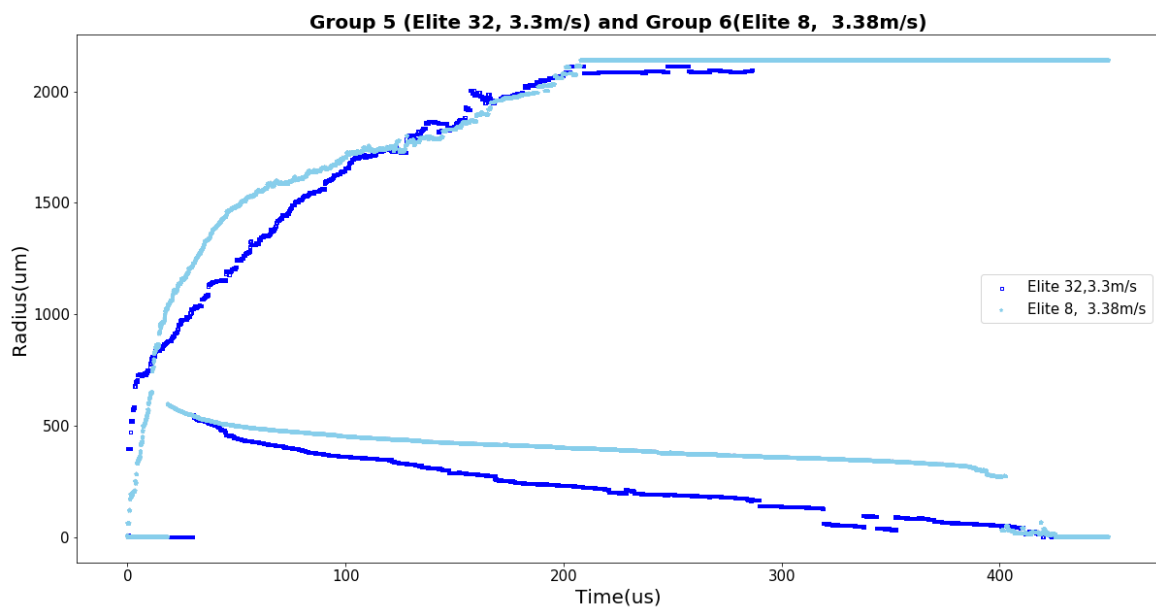
FIGURE C.3: Distance of the Contact Fronts from the Centers (Group 3 and Group 4) during the initial $500\mu s$ of impact process. The green color represents the Group 1 of Elite Doule 32 (E =1.1MPa) and impact velocity 2.46m/s. The lightgreen color represents the Group 2 of Elite Double 8 (E =250 KPa) and impact speed 2.44m/s.
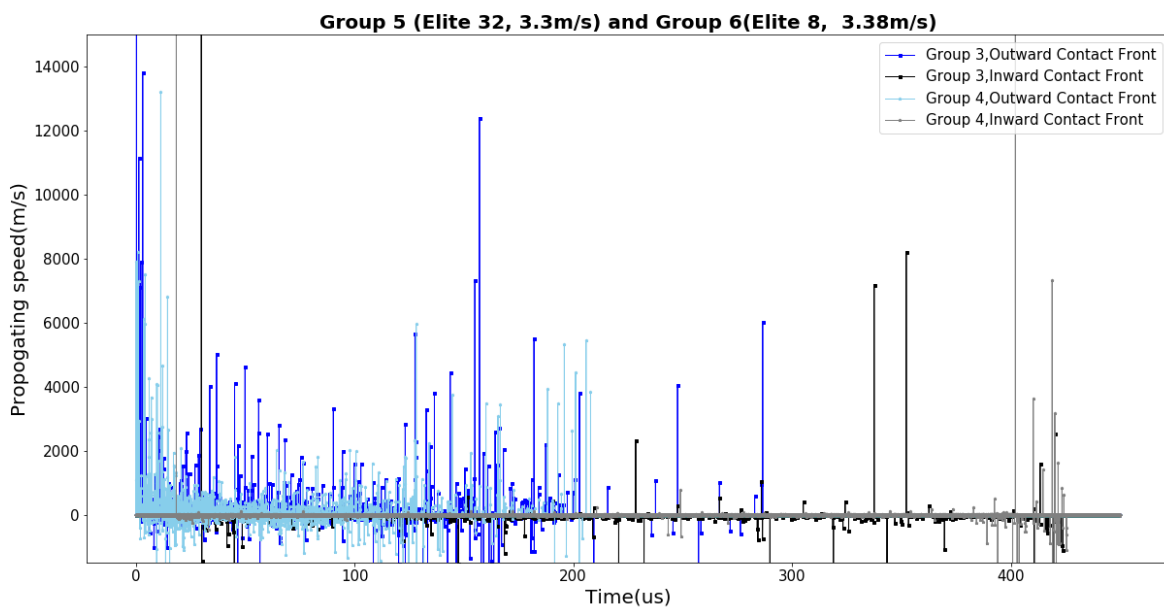
FIGURE C.4: Propagating speeds of the outward contact fronts (Group 3 and Group 4) during the initial $500\mu s$ of impact process. The green and black colors represent the outward and inward contact fronts in Group 1 of Elite Doule 32 (E =1.1 MPa) and impact velocity 2.46/s. The lightgreen and gray colors represent the outward and inward fronts in Group 2 of Elite Double 8 (E =250 KPa) and impact speed 2.44m/s.

FIGURE C.5: Distance of the Contact Fronts from the Centers (Group 5 and Group 6) during the initial 450μs of impact process. The blue color represents the Group 1 of Elite Doule 32 (E =1.1MPa) and impact velocity 3.3m/s. The lightblue color represents the Group 2 of Elite Double 8 (E =250 KPa) and impact speed 3.38m/s.

FIGURE C.6: Propagating speeds of the outward contact fronts (Group 5 and Group 6) during the initial 450μs of impact process. The blue and black colors represent the outward and inward contact fronts in Group 1 of Elite Doule 32 (E =1.1 MPa) and impact velocity 3.3/s. The lightblue and gray colors represent the outward and inward fronts in Group 2 of Elite Double 8 (E =250 KPa) and impact speed 3.38m/s.
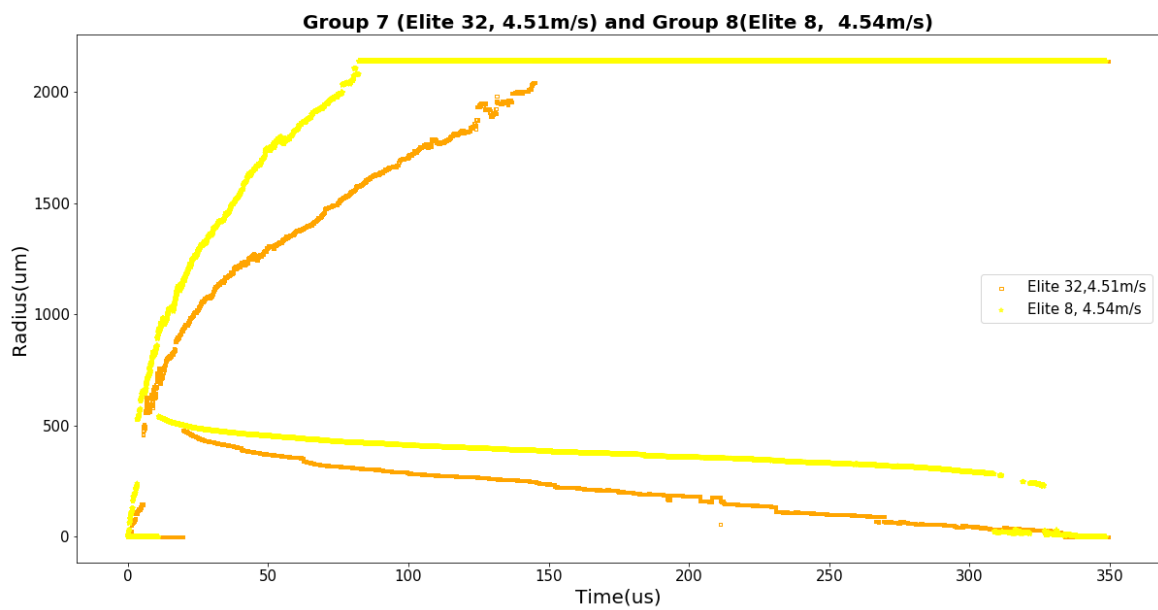
FIGURE C.7: Distance of the Contact Fronts from the Centers (Group 7 and Group 8) during the initial $350\mu s$ of impact process. The orange color represents the Group 1 of Elite Doule 32 (E =1.1MPa) and impact velocity 4.51m/s. The yellow color represents the Group 2 of Elite Double 8 (E =250 KPa) and impact speed 4.54m/s.
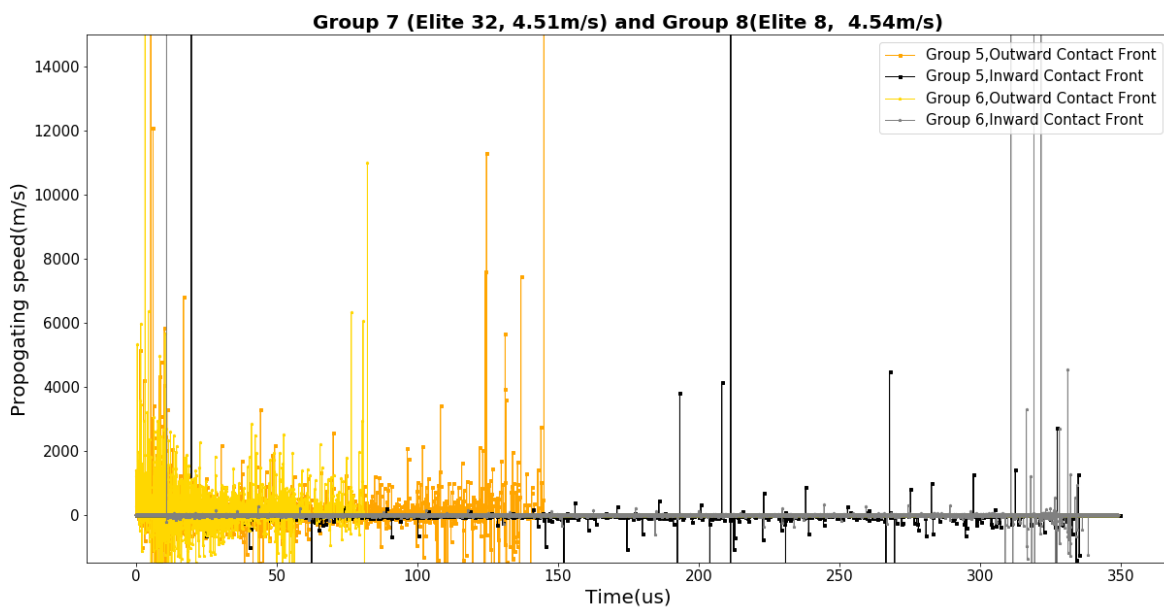
FIGURE C.8: Propagating speeds of the outward contact fronts (Group 7 and Group 8) during the initial $350\mu s$ of impact process. The orange and black colors represent the outward and inward contact fronts in Group 1 of Elite Doule 32 (E =1.1 MPa) and impact velocity 4.51/s. The yellow and gray colors represent the outward and inward fronts in Group 2 of Elite Double 8 (E =250 KPa) and impact speed 4.54m/s.
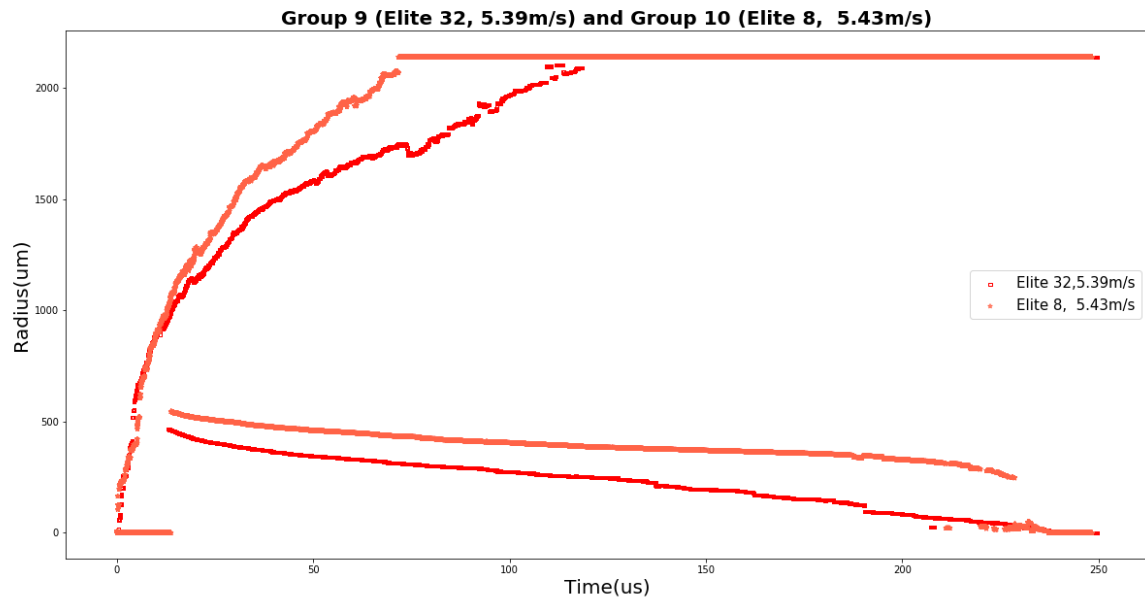
FIGURE C.9: Distance of the Contact Fronts from the Centers (Group 9 and Group 10) during the initial 250μs of impact process. The red color represents the Group 1 of Elite Doule 32 (E =1.1MPa) and impact velocity 5.39m/s. The lightred color represents the Group 2 of Elite Double 8 (E =250 KPa) and impact speed 5.43m/s.
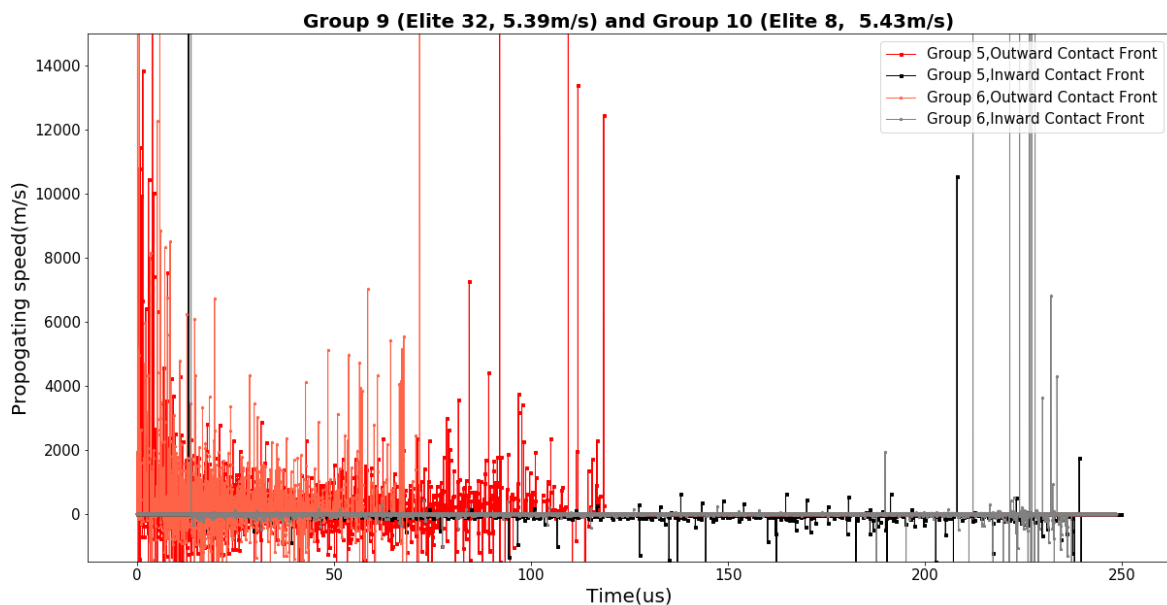

FIGURE C.10: Propagating speeds of the outward contact fronts (Group 9 and Group 10) during the initial 250μs of impact process. The red color represents the Group 1 of Elite Doule 32 (E =1.1MPa) and impact velocity 5.39m/s. The lightred color represents the Group 2 of Elite Double 8 (E =250 KPa) and impact speed 5.43m/s.
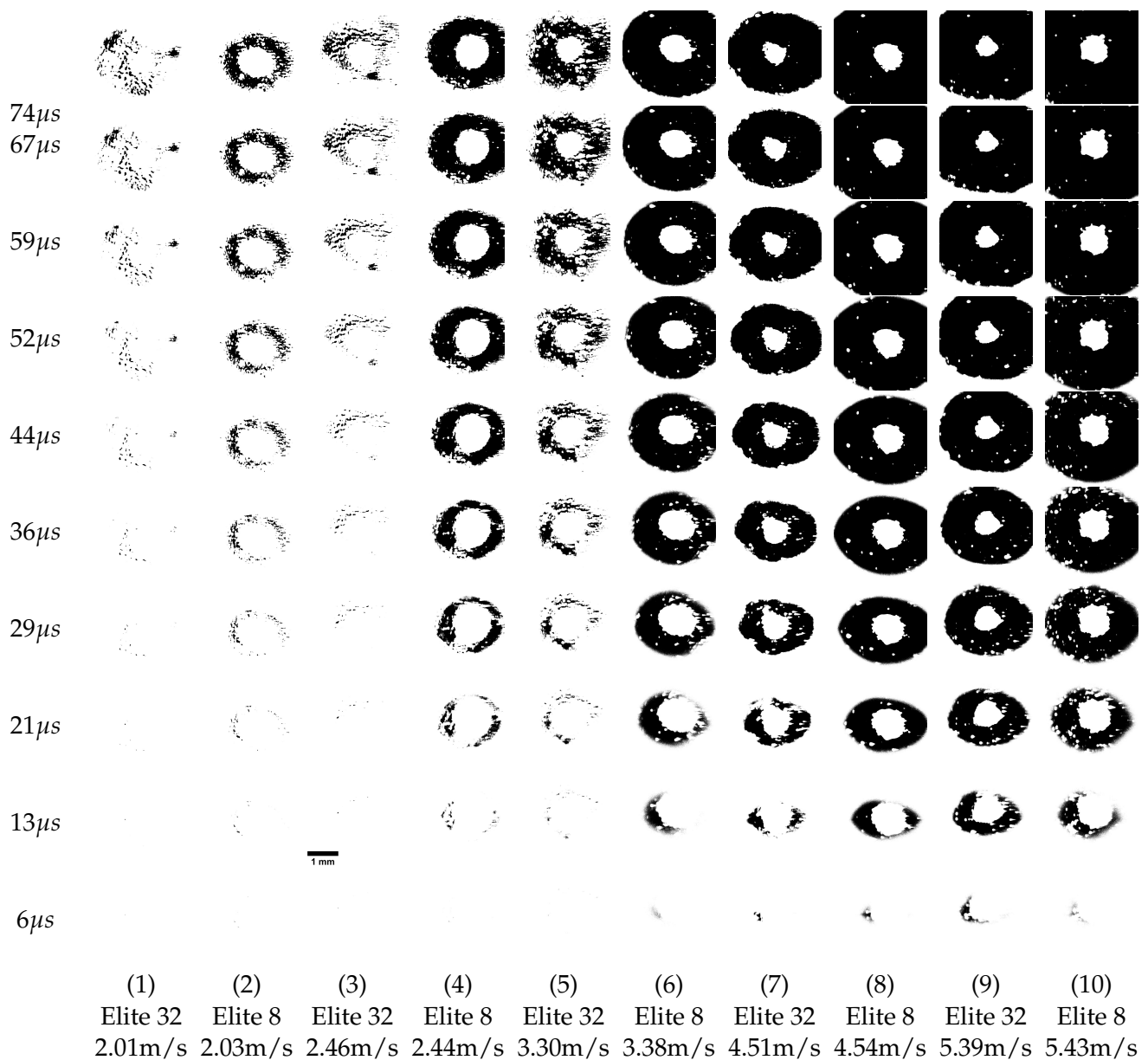
Appendix D

Virtual Frames of All Groups

FIGURE D.1: Some Virtual frames between $6\mu s$ and $74\mu s$ of each group. All the CFS are deconvolved to 65500 virtual frames.